Liquid Transport Rates during Binary Collisions of Unequally-sized Particles

Mingqiu Wu,[a,*] Johannes G. Khinast,[a,b] and Stefan Radl[a]

[a]Institute of Process and Particle Engineering, Graz University of Technology, Inffeldgasse 13/III, 8010 Graz, Austria

[b]Research Center Pharmaceutical Engineering GmbH, Inffeldgasse 13/III, 8010 Graz, Austria

*Corresponding author: E-mail: mingqiu.wu.ethtug@gmail.com; Tel.: +43 316 873 30417

Abstract

In this paper, we study the liquid transport between particles of different sizes, as well as build a dynamic liquid bridge model to predict liquid transport between these two particles. Specifically, the drainage process of liquid adhering to two unequally-sized, non-porous wet particles is simulated using Direct Numerical Simulations (DNS). Same as in our previous work (Wu et al., AIChE Journal, 2016, 62:1877-1897), we first provide an analytical solution of a proposed dynamic liquid bridge model. We find that such an analytical solution also describes liquid transport during collisions of unequally-sized particles very well. Finally, we show that our proposed model structure is sufficient to collapse all our direct numerical simulation data. Our model is hence able to predict liquid transport rates in size-polydisperse systems for a wide range of parameters.

Keywords:

Granular flows; Liquid transport; Polydisperse particle systems; Liquid bridge; Direct numerical simulation;

1. Introduction

Granular particle beds are usually composed of particles with different properties (i.e., shape, size, density, etc.[1]). It is well known that particle-size polydispersity and shape significantly influence the transport of mass and liquid in a fluidized bed [1,2] and spouted beds system [3]. Therefore, a better understanding of these systems (i.e., that involving particles of different sizes) helps to improve the control of many engineering applications, including fluidization, mixing, agglomeration, or coating. In addition, bi-and polydisperse fluidized bed systems often show a greater mixing performance [4–7]. Furthermore, other researches showed that wide particle size distributions result in smoother fluidization of dry systems [8–11]. Naturally, the question arises how polydispersity affects wet fluidized beds, i.e., three-phase systems in which a thin liquid layer (or droplets) is present on the particles' surface. In these systems two additional complications arise: (i) the prediction of the amount of liquid in each liquid bridge, and (ii) the magnitude of cohesive forces due to these bridges.

The rate of liquid bridge formation (i.e., the amount of liquid in the bridge as a function of time) plays an important role with respect to the bridge's rupture energy. Donahue et al [12] revealed that controlling the liquid bridge volume connecting two target particles is the key in obtaining the wet-collision results of their experiment. Thus, the amount of liquid present in the bridge is decisive if whether particles separate, or agglomerate [13]. Thus, it is important to quantify these interactions to predict the overall flow behaviour and the size of agglomerates in a fluidized bed. Although liquid transport processes between particles are always encountered in nature and in industrial applications [14–17], it is still difficult to quantify the associated transport rates of liquid. This is because the liquid transport between particles and the rate of exchange of liquid onto the particle surfaces is rather complex.

Next, we briefly review the latest development of liquid bridge formation in mono- and polydisperse particle beds. This is to motivate our present study that attempts to close the gap in understanding related to the rate of liquid bridge formation in systems involving unequally-sized particles.

Many researchers have studied the liquid-bridge and capillary-forces effects for monodisperse particle systems. For example, Hotta et al. [18], introduced a gorge method to calculate the capillary forces between particles by estimating the capillary force at the neck of the liquid bridge. Xu, et al. [19] employed a CFD-DEM approach to simulate a wet spouted bed of particles by using a static capillary force model. Mikami et al. [20] developed a bridge force

model between particles as a function of the dimensionless liquid bridge volume and separation distance based on numerical simulation of the Young-Laplace equation (YLE). Due to the complexity of using the YLE to describe the geometry of liquid surfaces, researchers introduced a toroidal approximation. This approximation treats the interface between liquid and air as a circular arc [21–24]. Another question is associated with the maximum separation distance for a stable liquid bridge. Therefore, Lian et al. [22] introduced a simple cube root relation between this rupture distance and the liquid bridge between equally-sized particles for small contact angles. However, all of this previous work assumes that the volume of liquid in the bridge is known – the effect of the initial liquid distribution (e.g., the liquid film present on the particles' surface) on the bridge volume is not modelled. Furthermore, all simple approximation methods assumed the meniscus of the bridge profile to be circular, and the liquid flow into the bridge was not predicted. Although some of these models assumed a zero contact angle when extracting the liquid bridge shape [25,26], the limitation of all these models is that the approximations are no longer correct for the liquid bride formation close to saturation. In these systems the liquid content is so high that the curvature of the gas-liquid interface and the Laplace pressure approaches zero [27]. In order to get the exact profile of the liquid bridge in these situations, one has to use numerical simulations to solve the YLE, or numerically solve the Navier-Stokes equations for a gas-fluid multiphase system. The latter approach also allows extracting the dynamic evolution of the gas-liquid interphase position, which provides data for building a dynamic bridge model. Only recently, our group [28] has employed such a simulation method based on the volume of fluid (VOF) approach to simulate liquid bridge formation. It allows a reconstruction of the interface deformation as a function of time, and ultimately to build a dynamic liquid bridge model. Such a model then provides a detailed and more rigorous understanding of how to predict liquid bridge forces in wet particulate systems.

So far, little attention has been devoted to wet polydisperse particle beds, especially with respect to the flow rate of liquid present on the particles' surface into the bridge. Orr et al. [29], were one of the first that studied liquid bridges with great rigor, and who derived a simple expression for the bridge shape and force (i.e., the adhesion force in contact with the sphere and the flat wall). Later, Willett et al. [24], provided a numerical solution for liquid bridge forces between spheres of equal and unequal radii, but still assuming the liquid bridge volume being known. In addition, Soulié et al. [30] proposed a similar capillary model for wet polydisperse granular materials based on the interparticle distance and the liquid bridge volume between two particles of different sizes. A similar approach has been used later by

Richefeu et al. [31]. Moreover, Sprakel et al. [27], provided a theoretical thermodynamic analysis of the capillary bridges between a sphere and a plate, as well as between spheres with equal or unequal particle size. This work considered both extremes, i.e., when the capillary bridge reaches the limit of saturation, and when the capillary bridge becomes very small. However, their work still considered a static situation, and the transient formation of the bridge was not considered. Recently, Chen et al.[32] presented a mechanical model for liquid bridges and the associated forces for two unequally-sized spherical particles, or a sphere and a flat plate. This study neglected gravitational effects, used the simple toroidal approximation to estimate the liquid bridge shape, and did not predict the dynamic filling of the bridge. The obvious drawbacks of all these approaches is that the liquid transport between particles and the flow of liquid into the liquid bridge has been neglected during the phase when particles approach each other.

To get an impression of different methods that have been employed for liquid bridge modelling, we next briefly summarize the methods that were used for studying liquid bridges. Essentially, there are two approaches: the first method is using simple approximation (i.e., toroidal approximation) based on the simplification of geometry [33–35]; the second approach solves the Young-Laplace equation (YLE) numerically [24], or analytically by solving a simplified YLE [22]. Only very recently, researchers started the simulation of liquid transport between two particles using a full solution of the Navier-Stokes equation [28,36,37]. Only the latter method provides a detailed description of the dynamic formation of the liquid bridge as shown in our previous work that used Direct Numerical Simulation (DNS) [28]. In this paper, we are going to extend our previous model to be valid as well for polydisperse particle systems.

1.1. Goals and Structure

In the current contribution we study the liquid bridge and liquid transport between two wet unequally-sized particles, i.e., we focus on particle-size effects on liquid bridge formation. We use a VoF-based Direct Numerical Simulation (DNS) approach to simulate both the motion of the liquid and the surrounding gas. We extend the method used in Wu et al. [28], to be available for bi-and polydisperse particle system. Our final goal is building a dynamic model to predict the liquid bridge volume during the filling process between these two unequally-sized particles. Thus, we fit our DNS data to a postulated liquid bridge filling model.

This paper is structured as follows: In Chapter 2 we describe the methodology used to establish the liquid bridge model, including (i) the setup and initial conditions that have been used in our simulations, (ii) the simulation approach and the gas-liquid interface extraction strategy, as well as (iii) the proposed model for the filling of liquid bridge. In Chapter 3, we introduce a geometrical bridge volume, which is used to normalize the bridge volume measured from our detailed simulations. In Chapter 4 we present the main results, starting with the calibration of the sub-models for the initial bridge volume and the subsequent viscous filling stage. Finally, we discuss our findings in Chapter 5, and provide conclusions that should guide the application and future extension of our model in Chapter 6.

2. Methodology

2.1. Setup and Initial Conditions

Two smooth particles of unequal sizes are fixed in space, i.e., their relative particle velocity is assumed to be zero. We define particle 1 to have a smaller radius than that of particle 2, and we fix the radius of particle 2 while varying the radius of particle 1 in what follows. We consider particles fully wetted, i.e., the two particles are initially fully covered by uniformly thick films. As shown in Figure 1, O_1 and O_2 are the two particle centres, R_1 and R_2 are the particles' radii, and h_1 and h_2 are the initial film thicknesses for particle 1 and particle 2, respectively. In the present work we consider systems in which h_1 and h_2, i.e., the dimensional film thicknesses, are equal for both particles. S is defined as the half separation distance between two particle surfaces. Moreover, we consider an axisymmetric liquid bridge, such that that we can perform corresponding two-dimensional simulations with adequate numerical resolution in a feasible time.

In addition, and as shown in Figure 1, the initial shape of the liquid bridge region (i.e., the green-shaded ring) has been set according to the initial film height, the separation distance and the particle radii. This is done considering the following line of thoughts: as we assume particles to be static, we cannot predict the deformation of liquid films on the particle surfaces before the films overlap. Therefore, we assume that liquid in the overlapping region (i.e., the black-shaded region in Figure 1) of the liquid films is instantaneously displaced. This liquid flows into a ring-shaped region (i.e., the green-shaded ring in Figure 1). Thus, we consider an initial bridge that has a cylindrical shape, and which dimensions are calculated purely based on geometric arguments. The calculation of this "geometrical bridge volume" for unequally-size particle is detailed below in section "Geometrical Bridge Volume".

Also, in our simulations there is no gravity, and no other forces act on the system. Consequently, there is only one physical reason why liquid residing in the films on the particle surfaces flows into the liquid bridge: the pressure in the film (adhering to the particle surface, and far away from the bridge) can be estimated as $p_{s,1} \approx 2\sigma/R_1$ for particle one, and similarly for particle 2. The pressure in the liquid bridge region, however, can be approximated as $p_{V_b} \approx -\sigma/R_{curve}$. Here R_{curve} is the radius of curvature of the liquid bridge surface. Thus, the relative pressure in the liquid bridge region is always negative or zero, while that in the film is always positive. Hence, a pressure difference between the particle

surface and the liquid bridge region exists, driving the liquid into the bridge. This liquid flow will not stop until the pressure difference reaches zero, or the liquid film on the particle surface ruptures.

In order to render the system dimensionless, we choose the following key dimensional reference quantities:

$$\begin{aligned} &R_{eff} = 2R_1R_2/\left(R_1+R_2\right); \quad t_{ref} = R_{eff}\mu_l/\sigma \\ &U_{ref} = \sigma/\mu_l; \qquad P_{ref} = \sigma/R_{eff}; \end{aligned} \tag{1}$$

Where R_{eff} is the effective particle radius, t_{ref} is a relevant reference time scale chosen to be the ratio of the effective particle radius and the capillary speed, U_{ref} is the velocity scale (i.e., the capillary speed), and P_{ref} is the pressure scale chosen (i.,e., a typical capillary pressure given by surface tension over the effective particle radius).

The key dimensionless parameters are then:

$$\begin{aligned} &h_1^+ = h_1/R_2;\ h_2^+ = h_2/R_2;\ h_0 = \left(h_1+h_2\right)/2;\ h_0^+ = h_0/R_2;\ S^+ = S/R_2, R_r = R_1/R_2 \\ &t^+ = t/t_{ref};\ L_{p1}^+ = L_{p1}/R_{eff}^3;\ L_{p2}^+ = L_{p2}/R_{eff}^3;\ L_{p,0}^+ = \left(L_{p1}^+ + L_{p2}^+\right)/2;\ V_b^+ = V_b/R_{eff}^3 \\ &\rho_{ratio} = \rho_l/\rho_g;\ \mu_{ratio} = \mu_l/\mu_g;\ Re = \sigma R_{eff}\rho_l/\mu_l^2;\ Oh = \mu_l/\sqrt{\rho_l\sigma R_{eff}} = 1/\sqrt{Re} \end{aligned} \tag{2}$$

Where, h_1^+, h_2^+ are dimensionless initial film heights for particle 1 and particle 2 respectively, and h_0^+ is the average film height, which quantifies the amount of liquid in the particle system. S^+ is the dimensionless separation distance, and R_r is the ratio of the small and large particle diameter; t^+ is the dimensionless time, L_{p1}^+, L_{p2}^+ and V_b^+ are the amount of liquid on the particles' surfaces and the bridge volume normalized with the reference volume (i.e., the effective particle radius cubed); ρ_{ratio} and μ_{ratio} are density and viscosity ratio between liquid and ambient gas, respectively. The Reynolds number *Re* is defined based on the capillary speed, fluid viscosity and the effective particle radius. *Oh* is an Ohnesorge number which is simply the inverse of the square root of the Reynolds number.

2.2. Simulation Approach and Liquid Bridge Volume Calculation Strategy

The simulations were performed using a Volume of Fluid (VoF) approach, specifically the implementation "*interfoam*" [38] in the open-source software package OpenFOAM®. The two-fluid flow is modelled with Navier-Stokes equation

$$\frac{\partial(\rho \boldsymbol{U})}{\partial t}+\nabla\cdot(\rho \boldsymbol{U}\boldsymbol{U})=-\nabla p+\mu\left[\nabla \boldsymbol{U}+(\nabla \boldsymbol{U})^{T}\right]+\boldsymbol{F}_{b} \quad (3)$$

$$\nabla\cdot \boldsymbol{U}=0 \quad (4)$$

Where $\boldsymbol{U}$ is the local velocity shared by the two fluids, it is subjected to the incompressibility constraint, ρ is local density, p is local pressure, and $\boldsymbol{F}_b$ are body forces, which include only surface tension effects at the interface in the present work. We stress that effects due to gravity have been neglected in our simulation, simply because viscous and capillary effects are dominant in situations involving relevant particle systems where particles have a diameters smaller than the capillary length.

We consider two immiscible fluids, i.e. gas and liquid, density and viscosity are constant in each phase, but can be discontinuous at the interface. We use a phase volume fraction indicator α in the transport equation of velocity field to represent the interface phase:

$$\frac{\partial \alpha}{\partial t}+\nabla\cdot(\boldsymbol{U}\alpha)=0 \quad (5)$$

The phase function α can proceed within the range $0<\alpha<1$, with alpha being zero (or unity) in regions occupied by the gas (or the liquid), respectively. The local average density and viscosity are computed from the volume fraction as:

$$\rho=\rho_l\alpha+\rho_g(1-\alpha) \quad (6)$$

$$\mu=\mu_l\alpha+\mu_g(1-\alpha) \quad (7)$$

Where ρ_l (or μ_l) and ρ_g (or μ_g) are the density (or the dynamic viscosity) of the liquid and gas, respectively.

We assumed that two particles with different sizes are completely wet, i.e., there is no three-phase contact line initially. Our preliminary results shown in Figure 5 suggest that the liquid transport process can be divided into three stages: a fast filling stage (i.e., $t^+<1$) in which the typical shape of the bridge is established; a viscous filling stage (i.e., $1<t^+<154$) and a post rupture stage (i.e., $154<t^+$). This is in line with our previous work on mono-disperse systems [28], in which we also observed film rupture on the particle with the thinner film. Note, we currently use the "*interfoam*" solver only for the first two stages: after the film gets ruptured, a three-phase dynamic contact line appears (see Figure 5, panel for t^+=154.7), and our solver will deliver inaccurate (but still physical) predictions of the liquid bridge shape post rupture

[28]. To circumvent this problem, we did not consider data collected after film rupture events in our analysis. Again, this is in line with our previous work [28]. All relevant simulation parameters and numerical schemes are listed in Table 1.

The liquid-gas interphase can be easily determined from the DNS data by analysing the distribution of the phase fraction. Consequently, the interface position can be determined at α = 0.5. Hence, we have taken a simple, yet effective sampling method to detect the gas-liquid of the film and the bridge formed between the particles.

As can be seen in Figure 5 (zoomed region for $t^+ = 1.33$ indicating the liquid velocity), liquid from the small particle surface is transferred faster into the bridge than from the bigger one. Thus, the liquid film on the upper (smaller) sphere is no longer spherical-shell shaped, but quickly deforms into a complex shape. Therefore, and in order to get accurate data, we will not just sample along the distance between O_1 and O_2 as shown in Figure 2 as we did in previous work [28]. Instead, we use a sampling procedure which takes place from the top pole of particle 1 to the bottom of particle 2 with an interval of Δx and a large enough maximum sample distance δ (see Figure 2). By doing so, we obtain a list of data for the phase value along each sampling line, and subsequently the interface position. We then need to define which portion of the fluid in the system is considered to be in the liquid bridge. This is done by using the same approach as used in our previous work [28], and which considers the following line of thoughts: in case one would analyze the thickness profile on each particle, one can observe a certain angular position where the film is thinnest. We have used this local minimum to mark the extent of the liquid bridge. Specifically, we denote these positions of the minima as the “neck” positions, which separate the bridge from the film adhering to the particle surface. Clearly, in case the film ruptures, this will happen at these neck positions. After the interface positions and neck position have been determined, we can calculate the liquid bridge volume by using a direct integration method (DIM) presented in our previous work [28].

2.3. Proposed Model for Liquid Bridge Filling

The DNS of liquid flow on unequally-size particles during their collision indicates that the mechanism of liquid bridge formation consists of the following steps: first the liquid-covered particles approach each other. Then, the films coalesce, a liquid bridge is formed between the particles, and finally liquid drains into the bridge. Ultimately, film rupture may occur, which is not considered here in greater detail. Thus, similar to our previous work [28] it is

reasonable to differentiate between two stages of the filling process of liquid bridge: (I) a capillary-force driven initial stage (fast filling), and (II) a viscous filling stage (slow filling). We define stage I to end after a (viscous) reference time scale of t_{ref}, i.e., a dimensionless time of t^+=1, was reached. This reference time in Equation (1) is different from that in the monodisperse system by definition, as the effective particle radius affects the reference time scale.

As shown next, we employ two different sub-models to predict the liquid bridge volume in each of these two stages. By employing an overall mass balance it is then straightforward to predict the liquid residing on the contacting particles. Specifically, for the initial stage, we aim to correlate the bridge volume at $t^+ = 1$ with the most important process parameters. Therefore, we choose the key geometrical parameters, which are (i) the average initial film height h_0 , (ii) the half separation distance S and (iii) the particle seize ratio R_r.

Our model to predict the time evolution of liquid bridge volume in stage II ($t^+ > 1$) is the same as reported in our previous work [28], extended to account for unequally-sized particles. Specifically, we use a phenomenological closure for the flow rate between the film and the bridge compartment. We assume the flow rate to be proportional to the difference of the mobile fraction of the liquid on the particle, and half of the bridge volume. Moreover, we define a mobility parameter $\phi_{m,i}$ to predict the mobile fraction of liquid presented on particle surface. This parameter is the ratio of the liquid mobile to flow on the particle i's surface, divided by the total liquid content on particle i. In Chapter 4 we show that the mobility parameter is a function of the initial film height and the particle separation, as well as the particle size. For what follows we accept $\phi_{m,i}$ as a time-independent parameter that is fixed during the filling process. Next, we introduce a dimensionless filling-rate parameter a_i (which one can assume to be specific for each particle i), as well as a reference time scale t_{ref}. We then postulate a simple differential equations for predicting the liquid content $L^+_{p,i}$ on each particle i which reads:

$$\begin{aligned} \frac{dL^+_{p1}}{dt^+} &= \frac{-a_i}{t_{ref}}\left(L^+_{p1}\phi_{m1} - \frac{V^+_b}{2} \right) \\ \frac{dL^+_{p2}}{dt^+} &= \frac{-a_i}{t_{ref}}\left(L^+_{p2}\phi_{m2} - \frac{V^+_b}{2} \right) \end{aligned} \qquad (8)$$

$$\frac{dV_b^+}{dt^+} = -\left(\frac{dL_{p1}^+}{dt^+} + \frac{dL_{p2}^+}{dt^+} \right) \quad (9)$$

Appropriate initial conditions, as well as the assumption that a_i is a constant for a pair of particles sharing the same bridge, lead to the analytical solution documented in appendix A of our previous work [28].

3. Geometrical Bridge Volume

The goal of this paper is to study liquid bridge formation between two unequally-sized particles, and hence it is useful to define a reference bridge volume based on some geometrical arguments. Therefore, we choose the precise geometrical bridge volume (this corresponds to "model II" in our previous work [28]) as the reference bridge volume. This volume is used to normalize the early stage model for the liquid bridge volume (see our "Results" section). This geometrical bridge volume is calculated by assuming the liquid in the overlap region (see black-shade region in Figure 1) to be displaced when particles approach each other. Liquid in the overlap region is assumed to flow into a ring-shaped area (see Figure 1; more details on the calculation are available in our previous work [28], and are not repeated here for brevity). This evaluation of bridge volume requires an iterative procedure, which makes it more expensive and less attractive for larger-scale DEM-based simulations. However, the bridge volume defined in such a way is more accurate, as it is closer to our results of the DNS as we will demonstrate in or "Results" section below.

We next highlight some trends of the geometrical bridge volume of an unequal-size particle pair, and how this volume is affected by the particle size ratio, the separation distance, and the initial film height. The subsequent figures and text, $V_{b,g}$ is the type II geometrical bridge volume as introduced in previous work [28]. Figure 3 shows that the normalized particle size (i.e., R_r) and the separation distance have a significant effect on the bridge volume, as indicated by Figure 3 (black triangles and blue cycles). Also, the bridge volume increases monotonically, but non-linearly, with increasing (initial) liquid content for every choice of separation distance. Also, it can be observed that the bridge volume decreases with increasing separation distance, finally approaching zero for $S^+ = h_0^+$ as it should be. The physical interpretation of this fact is that for the situation in which the separation equals the initial film thickness, the overlapping region of a thin film between two particles vanishes. We also can see from the figure that particles with identical size and larger separation distance (i.e., R_r = 1,

light-green diamonds) have smaller bridge volumes compared to smaller particles at zero separation (red triangles shown in Figure 3). Again, this highlights the strong effect of the separation distance on the liquid bridge volume. Interestingly, at identical (dimensionless) separation, mono-disperse particles (i.e., R_r = 1, light-green diamonds) imply a larger dimensionless liquid bridge volume than particles of different size (i.e., R_r = 0.5, black squares).

Figure 4 (panel b and c) shows the general behavior of the dimensionless geometrical bridge volume as a function of the particle size ratio. Thus, the key message of this figure is that the (normalized) bridge volume decreases when the particles become more identical in size, i.e., R_r approaches unity.

Another key observation is that for extremely small particle size ratios and thick films our definition of a geometrical bridge volume breaks down. Panel (a) illustrates these limiting conditions for the geometrical bridge calculation: the first obvious limit is that the radius of the smaller particle (i.e., particle 1) plus the distance between two particle surfaces must be larger than the initial film height of the larger particle (particle 2). Thus, we require $R_1 + 2S > h_2$, and hence we must ensure $R_r > h_2^+ - 2S^+$ in order to compute a meaningful geometrical bridge volume. Since the smaller particle would be completely immersed in the liquid layer of the larger particle otherwise, we call this limit the "immersion limit". The second limit is imposed by the radius R_{cyl} of the ring-shaped region of the liquid bridge (i.e., the region shaded in green in Figure 1). In case R_{cyl} is larger than $R_1 + h_1$, it is also not possible to define a geometrical bridge volume. This is simply because the assumption of ring-shaped (cylindrical) liquid bridge is no longer consistent with the geometrical arrangement of the particles and the films. Hence, we denote this critical situation as the "ring radius limit".

Panel (b) in Figure 4 shows the change of the bridge volume for particles ratios from 0.1 to 1 with different initial film heights and zero separation distance. For all these figures the limiting size ratio for the "immersion limit" discussed above has not been reached. Still, the normalized liquid bridge volume can reach values close to unity, and varies significantly with R_r. This indicates that the relative size ratio is a key influence parameter when estimating the liquid bridge volume.

In contrast, panel (c) shows the bridge volume for particle size ratios ranging from 0.02 to 0.05 with larger separations. In this case neither the "immersion limit", nor the "ring radius limit" has been reached. A large value of the dimensionless (geometrical) liquid bridge

volume indicates that for these situations the collision approaches the limit of a collision in which both particles are fully immersed in a liquid. While it was impossible to simulate such extreme diameter ratios as shown in Figure 4c in the present contribution, we speculate that the exact details of the bridge shape are irrelevant for these situations. This is simply because of the above mentioned argument connected to the large dimensionless bridge volume, which effectively has the physical meaning of a collision occurring fully immersed in the liquid phase.

4. Results

4.1. Early Stage Model

As illustrated in Figure 2, the initial bridge forms very quickly and the inertia of the fluids (i.e., that of the liquid and the surrounding gas) plays an important role. Due the difficulty to model the inertial effects in our analytical model, we hence define a fixed initial bridge volume for "early times". Specifically, we choose one reference time at t^+=1 as the "early time". We then attempt to model the initial bridge volume by defining the variable K_{v1}, which is the value of the total simulated bridge volume at t^+=1, demarcated as ($V_{b,0}^+$), over the particle ratio R_r to the power of some exponent m and the average initial film height h_0^+ to the power of some exponent n:

$$K_{v1} = \frac{V_{b,0}^+}{R_r^m \left(h_0^+\right)^n} \qquad (10)$$

This definition is based on the idea that the initial bridge volume is some function of the (initial) film height and the ratio of the particles' radii. Thus, there is no need to compute the geometrical bridge volume defined above. Instead, we hope that appropriate exponents in Eqn. 10 lead to a collapse of our data for $V_{b,0}^+$. Indeed, we can see from our data shown in Figure 6 that this ansatz reasonably collapses our DNS results with a linear model once we choose m and n correctly: firstly, by choosing m = -1.25 and normalizing the initial bridge only with the term originating from the particle size ratio R_r, we observe three groups of data based on the initial film height (see Figure 6, panel a); secondly, by choosing n = 2.15 and only normalization the bridge volume using the term origination from the initial film height h_0, we can see the collapsed DNS data forms three groups based on different values for R_r (see panel b in Figure 6); finally, by combining panel a and b, i.e., normalization with both

terms in the denominator in Eqn. 10, we arrive at the final model illustrated in panel c. The error of this fitted model shown in equation (11) is around 8%, which is also illustrated in panel c of Figure 6.

$$K_{v1} = -8.2\frac{S^+}{h_0^+} + 50.8 \qquad (11)$$

From equations (10) and (11) we can now formulate the final expression for $V_{b,0}^+$:

$$V_{b,0}^+ = R_r^{-1.25}\left(h_0^+\right)^{2.15}\left(-8.2\frac{S^+}{h_0^+} + 50.8\right) \qquad (12)$$

This model is comparable to our model for the monodisperse particles system ([28]; for a monodisperse particle system the particle size ratio R_r is 1). Then, equation (12) can be simplified to

$$V_{b,0}^+ = \left(h_0^+\right)^{2.15}\left(-8.2\frac{S^+}{h_0^+} + 50.8\right) \qquad (13)$$

We have confirmed that we obtain a comparable initial bridge model by comparing this new result to our previous results for monodisperse systems [28]. Thus, Eqn. 13 is simply a more rigorous form of our previous work only valid for $R_r = 1$.

In summary, our model for K_{v1} given by Eqn. 12 could already be used to compute $V_{b,0}^+$ for short collisions (or collisions involving very viscous liquids) between two unequally-sized wet particles. In these situations the amount of liquid draining into the bridge would be negligible compared to that formed simply due to the squeezing of the liquid by the approaching particles. Most important, the model presented in Eqn. 12 does not require an iterative numerical evaluation of the geometrical bridge volume, but simply the rather computationally efficient evaluation of two power law functions, as well as some additions and product evaluations.

Despite this, we next still aim on using the detailed geometrical bridge volume to normalize the simulated initial bridge volume. We do this since this model already accounts for the effect of the separation distance and film height on the bridge volume. Thus, we expect that normalization with the geometrical bridge volume yields an even simpler model for the bridge volume. By doing so, we define the variable K_{v2} as the ratio of the simulated initial bridge volume, the geometrical bridge volume, the particle ratio, and h_0^+:

$$K_{v2} = \frac{V_{b,0}^{+}}{V_{b,g}^{+} R_r^m \left(h_0^{+}\right)^n} \quad (14)$$

Again, m and n are parameters that are used as exponents of the particle ratio and initial film heights, respectively, helping to collapse all data into a single curve. V_{bg} is the "type II" geometrical bridge volume introduced in our previous work [28]. The result of our analysis is displayed in Figure 7, indicating that we can fit the collapsed data to a parabolic function. This model is a bit different from the monodisperse system (the monodisperse system has been fitted as linear function): However, the exponent of the initial film heights has been chosen again as $n = 0.2$ (in line with our model for the monodisperse system reported in [28]), which collapses all initial film heights. By choosing $m = 0.4$ for the exponent of the particle size ratio, we suggest a parabolic relationship between the normalized liquid bridge volume and the separation distance:

$$K_{v2} = 1.4\left(\frac{S^{+}}{h_0^{+}}\right)^2 + 2.4 \quad (15)$$

The error for this model is around 8%, which can also be seen from Figure 7. Hence, the expression for the initial bridge volume $V_{b,0}^{+}$ is:

$$V_{b,0}^{+}/V_{b,g}^{+} = R_r^{0.4}\left(h_0^{+}\right)^{0.2}\left(1.4\left(\frac{S^{+}}{h_0^{+}}\right)^2 + 2.4\right) \quad (16)$$

We again can obtain the model for the monodisperse particle system in case we set R_r equal to 1, which yields

$$V_{b,0}^{+}/V_{b,g}^{+} = \left(h_0^{+}\right)^{0.2}\left(1.4\left(\frac{S^{+}}{h_0^{+}}\right)^2 + 2.4\right) \quad (17)$$

Although the model here is a parabolic function which is different from our previous work on monodisperse particle systems [28], the exponent n for the initial film height still equals 0.2. This exponent is identical to the one we previously used for monodisperse particle systems.

In summary, the model for K_{v1} and K_{v2} presented above can be used to calculate the bridge volume at t^{+}=1. We next focus on the calibration of parameters in the proposed viscous bridge-filling stage. This stage can be used to predict the time evolution of the liquid bridge at longer times, for which viscous effects play a significant role.

4.2. Viscous Filling Model

We now consider the time evolution of the bridge volume and the liquid present on particles' surface, and how this is affected by different parameters (see Figure 8). Based on this data, we obtain the mobility parameters (defined in Section 2.3) by running the simulations to a dimensionless time of $t^+ = 100$. We have used a mesh size of $\Delta h = \Delta x / h_0 = 0.1$. We find that cases initialized with $h_0 = 0.04 \cdot R_2$ exhibit film rupture at dimensionless evolution times equal to approximately 100 with this mesh size. Film rupture still does not happen at this time for cases with larger initial film heights (i.e., $h_0 = 0.06 \cdot R_2$ and $h_0 = 0.1 \cdot R_2$), and even after $t^+ = 1000$ w do not observe film rupture for these cases. However, data between zero and $t^+ = 100$ already provides us with enough data to fit our dynamic model.

Specifically, we obtain the parameters $\phi_{m1} = 0.66$, $\phi_{m2} = 0.22$ for Figure 8a, and $\phi_{m1} = 0.2$, $\phi_{m2} = 0.14$ for Figure 8b. Thus, we find that the mobility parameter of particle 1 is larger than that of particle 2 (note, particle 1 has a smaller particle size than particle 2). Physically, this means that more liquid drains from the smaller particle, consistent with the simple arguments based on the higher capillary pressure on particle one discussed in Chapter 2.1. Furthermore, we find that the dimensionless filling rate coefficient a_i for long times (i.e., $t^+ = 100$) is approximately 0.01. This value fits all our data reasonably well for the chosen evolutional time of t^+=100. Hence, we accept a_i to be a universal constant from now on.

Figure 9 shows a test of our model for other combinations of particle size ratios, initial film heights and separation distances. These results reveal that our model is indeed able to describe the filling process well. Also, we can observe from Figure 9a that larger initial film heights always lead to a larger bridge volume. From Figure 9b we see that smaller particle size ratios always lead to larger dimensionless bridge volumes. This is due to the fact that the reference volume is smaller (i.e., the effective particle diameter is smaller), and consistent with our simple model for the geometrical bridge volume presented in Chapter 3.

Additionally, we can see that the filling process levels off after about 100 dimensionless time units. This time unit is also suggested by the inverse of the constant a_i which has been fixed before. A time of 100 is long enough for most cases, as the filling process is almost completed and in most cases, thin films have already ruptured at this point in time. Therefore, using the current coefficient $a_i = 0.01$ seems more appropriate, compared to the value of 0.025 that we previously reported for the monodisperse cases [28]. One reason for this difference is that in

the current contribution we have run the simulations for longer times. Also, it appears that the particle size ratio has a subtle effect on the liquid drainage rate: our model (with a_i = 0.01) tends to undepredict the DNS data for increasing R_r (see the data reported in panel b of Figure 9), and hence one might want to use the somewhat larger value for a_i for monodisperse systems as suggested in Wu et al. [28].

We now aim to demonstrating that our model is able to represent data for a variety of dimensionless initial film heights, particle size ratios and separation distances. Therefore, we have collected the mobility parameters by fitting the data from a large array of DNS. Also, we now make an attempt to model ϕ_{m1} and ϕ_{m2} separately. Equation 18 defines the variable $K_{\phi_{m1}}$ as the ratio of the mobility coefficient of particle 1 (i.e., ϕ_{m1}), the particle size ratio R_r, and the initial (average) film height h_0.

$$K_{\phi_{m1}} = \frac{\phi_{m1}}{R_r^m \left(h_0^+\right)^n} \qquad (18)$$

Here, m and n are some exponents of the particle size ratio and the average initial film height, which help to collapse the data into one curve. When picking m = -2 and n = 2, we obtain a model for $K_{\phi_{m1}}$ which is supported by our data shown in Figure 10, and which reads:

$$K_{\phi_{m1}} = 100\left(1 - 0.48\frac{S^+}{h_0^+}\right) \qquad (19)$$

The error for the model K_{ϕ_1} is about 13%, which can also be seen from Figure 10. In summary, and by combining equations (18) and (19), one can now calculate the mobility coefficient ϕ_{m1} from the particle size ratio R_r, the average film height h_0^+ and the separation distance S^+ as:

$$\phi_{m1} = 100\, R_r^{-2}\left(h_0^+\right)^2\left(1 - 0.48\frac{S^+}{h_0^+}\right) \qquad (20)$$

Specifically, in case the particle size ratio R_r equals unity (i.e., we consider a monodisperse particle system), we can simplify equation (20) as function of average initial film height and separation distance.

Similarly, we can define a variable $K_{\phi_{m2}}$ to collapse our data for the mobility coefficient of particle 2:

$$K_{\phi_{m2}} = \frac{\phi_{m2}}{R_r^m \left(h_0^+\right)^n} \qquad (21)$$

Here, m and n are again parameters that are used as exponents of the particle ratio and average initial film height to collapse all our data for the mobility coefficient into a single curve. In order to be consistent with the mobility coefficient computed for particle 1 in the limit $R_r = 1$, we must choose $n = 2$. Then, by choosing $m = 0.62$, we collapse all our data for K_{ϕ_2} as shown in Figure 11, and propose the following closure relationship for it:

$$K_{\phi_{m2}} = 100\left(1 - 0.48\frac{S^+}{h_0^+}\right) \qquad (22)$$

The error for the model K_{ϕ_2} is about 13%, which can also be seen from Figure 11. Again, we have ensured consistency for the limit $R_r = 1$ by using the same factors in Eqn. 19 and 22. In summary, we can calculate the mobility coefficient of particle 2 for a known particle size ratio R_r, an average film height h_0, and a certain separation distance via:

$$\phi_{m2} = 100\, R_r^{0.62} \left(h_0^+\right)^2 \left(1 - 0.48\frac{S^+}{h_0^+}\right) \qquad (23)$$

Again, for particle ratio $R_r = 1$, we can simplify the above model and arrive at a closure relationship that is consistent with that of a monodisperse particle system. This indicates that the mobility coefficient of both particles is only function of the average initial film height and the separation distance, same as in our previous work [28]. Note, that we have not added the difficulty to consider different film heights on the particles in the present work. However, such an extension is rather straight forward.

In summary, we presented a model for the liquid mobility that describes liquid transfer from the particle surfaces to the liquid bridge. The model describes all our results for various particle size ratios, average initial film heights and separation distances by appropriate scaling using some exponents to these parameters. For specific cases, i.e., when R_r equals unity (i.e., a monodisperse system is considered), we find that the present model is slightly different from our previous model reported for monodisperse systems [28]. The reason for the differences is that we currently collect data for longer times (i.e., t^+=100), which we could not do in our previous study [28].

4.3. Film rupture and Driving Pressure

It is interesting to consider the pressure distribution in the film near the film rupturing event. From Figure 12 it can be seen that thin film always ruptures at the neck position with the current mesh ($\Delta h = 0.1$) for a sufficiently long times. Additionally, we can see in Figure 12 that thin films always rupture on the surface of the smaller particle (i.e., particle 1) for all cases. The reason is that the pressure difference between particle 1 and the bridge region is always larger than the one between particle 2 and the bridge region. Clearly, this is due the smaller radius of particle 1 that causes a higher curvature and pressure in the corresponding film: by using Young-Laplace equation, the pressure on particle 1 can be approximated as $P_1 = 2\sigma / R_1$, while $P_2 = 2\sigma / R_2$, and $R_2 > R_1$, resulting in $P_1 > P_2$. We can also confirm these findings in the pressure plots shown in Figure 12. Unfortunately, we could not precisely predict the processes after film rupture, since we did not employ a sound model for the contact line motion (i.e., we currently only consider a fixed contact angle). Although we speculate that these processes are still predicted qualitatively correct, this fact does not allow us to establish a model after the film rupturing event. Since our model currently is only based on data before the film ruptures, and data post film rupture is discarded, this appears to be unproblematic.

5. Discussion

In this study, we focus on liquid transport between two unequally-sized spherical particles based on key parameters (i.e., particle radius, initial film height and separation distance). We also provide a model for the prediction of dynamic liquid-bridge formation between particles of different sizes, by assuming a quasi-static flow situation which is based on the assumption that particle relative motion does not affect the liquid bridge formation. As demonstrated in our previous work [28], one can perform a time scale analysis to obtain a quantitative understanding of situations in which such a quasi-static assumption is appropriate. In the following we consider a sedimenting bi-disperse particle population, and summarize the most important findings of such a time scale analysis.

Compared with the larger particle (i.e., particle 2), the smaller particle (i.e., particle 1) will accelerate more rapidly because of its lower particle volume. Thus, we use the effective scales associated with particle 1 to characterize the system. When considering the acceleration of particle 1 due to surface tension forces, it is obvious that the characteristic time scale (denoted

as t_{acc}) for the particles to accelerate to a typical speed of liquid flow (i.e., $u_{ref} = \sigma / \mu_l$) must be larger than the time scale for liquid bridge formation to justify the quasi-static assumption for bridge filling. Also, the time for the particle to cross the film (denoted as t_{cross}) must be larger than the time scale for liquid bridge formation. t_{acc} can be calculated from a force balance on a particle by assuming that the liquid bridge only exhibits a cohesive force due to surface tension, and that the particle accelerates to u_{ref}. The corresponding dimensionless acceleration time scale (with $t_{ref} = R_{eff}\mu_l/\sigma$ being the reference time scale) is $t_{acc}^{+} = R_1^2\rho_p\sigma/\left(R_{eff}\mu_l^2\right) = R_1\rho_p\sigma\left(R_r+1\right)/\left(2\mu_l^2\right)$, where $R_{eff} = 2R_1/\left(R_r+1\right)$ and $R_r = R_1/R_2$. The time for a particle to cross the film can be calculated from a typical particle-particle relative velocity u_{rel} and the film thickness, i.e., $t_{cross} = h_0/u_{rel}$. The corresponding dimensionless crossing time scale (with the Stokes setting velocity as relative velocity) is $t_{cross}^{+} = 9h_0\mu_g\sigma/\left[2R_1^2R_{eff}\mu_l\left(\rho_p-\rho_g\right)g\right] = 9h_0^{+}\mu_g\sigma\left(R_r+1\right)/\left[4R_1^2R_r\mu_l\left(\rho_p-\rho_g\right)g\right]$, where h_0^{+} is the average dimensionless film-thickness (with R_2 being the reference length), μ_g is the ambient gas viscosity, and ρ_p is the particle density.

In summary, the assumption of no-moving particles in our simulations requires that both dimensionless time scales are much larger than unity. Following our previous work [28], and using typical properties of various water-glycerine mixtures summarized in Table 2 [39], we have summarized these key dimensionless parameters in Table 3. While situations with highly viscous fluids (i.e., pure glycerine) appear to conflict with our quasi-static assumption, Table 3 highlights that for most systems involving liquids with a water-like viscosity our quasi-static assumption is valid. This is in line with previous findings in mono-disperse systems [28].

The typical relative velocity at impact plays an important role in our analysis of the time scale for film crossing. Similar to what we have done in our previous work [28], we now consider systems of different particle sizes. The bi-disperse suspension is allowed to freely sediment (under the action of gravity), and the speed and orientation of particle-particle collisions is recorded. The simulations were based on the approach used by Radl and Sundaresan [40] (a dimensionless grid resolution of $\Delta x / d_p = 3$ was used, where d_p is the diameter of the larger particles), with identical fluid, but different particle properties. The soft-particle Euler-Lagrange model available in the code CFDEM® [41] has been used, and statistics were collected over a sufficiently long time, i.e., 40 times of the particle relaxation time

($t_{relax} = u_t / g$). A list of simulation parameters and conditions is provided in table 4, and results are summarized in Figure 13. We find that the typical impact speed is in the order of 10% of the particles' terminal settling velocity, and that particle collisions are primarily oblique (i.e., the particles' relative speed in the tangential direction is greater than that in the normal direction). Again, this data supports our assumption of quasi-static bridge filling for a wide range of wet bi-and polydisperse particulate system with rather thick liquid films and a rather low liquid viscosity.

One could argue that the relative speed of particles in a wet collision event is depending on the process. We have only considered a fluidized bed without cohesive particle-particle interactions in our present contribution. It is clear that the appropriateness of our model for a specific application (which might involve cohesive forces, or much different collision dynamics) should be tested prior to its usage. We have decided to postpone such a study to future work, since a large array of simulation would have to be performed for bi- and polydisperse suspensions in order to draw general conclusions.

6. Conclusions

A liquid transport model between wet particles of different size has been presented in this paper. This model is an extension of our previous work [28]. The model is based on DNS data which were obtained by extracting the interface position, defining the characteristic neck position, and integrating the interface position to quantify the liquid bridge filling process. This model allows us to predict the dynamically evolving liquid bridge volume, and the liquid remaining on the particle surfaces in polydisperse particle systems. Our more precise prediction of the bridge volume is essential for improved predictions of the liquid bridge rupture energy: a comparison of these differences when using the liquid bridge volume model of Shi and McCarthy [42] and our newly developed model reveals large differences for the rupture energy (see Appendix A). Thus, we expect that our dynamic model for the liquid bridge volume is especially important for dilute systems where energy dissipation during collisions is of critical importance.

Our model differentiates between (i) a fast initial bridge formation stage where the dimensionless time is less than a reference time for capillary-driven viscous flow, and (ii) a subsequent slower viscous filling stage where viscous effects are dominant. The initial stage model is based on DNS data at a dimensionless time of $t^+ = 1$. Our initial stage model can be

used as a first estimate for the liquid bridge volume in short particle collisions, and is an extension of the model prosed by Shi and McCarthy [42]. The postulated model for the viscous filling stage model is an extension of our previous work [28], however now is also fit for systems involving unequally-sized particles. Our present model relies on a universal parameter a_i (i.e., a characteristic dimensionless filling time), as well as dimensionless liquid mobility parameters ϕ_{m1} and ϕ_{m2} of the contacting particles. A model equation for these mobility parameters has been proposed. Specifically, we consider that the mobilities are functions of the particle size ratio, the film height and the separation distance. In summary, our model is valid for liquid bridge formation between two unequally-sized particles coated with thin continuous films (i.e., an initial relative film height of less than 10% of the particle radius).

Our previous study indicated that grid refinement plays an important role in the final stages of film flow where the film ruptures. In order to get a precise model for the filling process at long times, as well as to correctly predict film rupture, it is essential to use a fine enough computational mesh in future simulations. This clearly limited the current study to axisymmetric configurations. Consequently, considering non-continuous films, e.g., discrete droplets present on the particles' surface, remains a task for future studies. However, we hope that our study is a significant step forward to better understand the equilibration of liquid residing on the surface of particles with that present in a liquid bridge.

Acknowledgement

We acknowledge the funding of the FWF through project P23617, as well as WKP 67. Also, we gratefully acknowledge support from NAWI Graz by providing access to dcluster.tugraz.at. OpenFOAM® is a registered trademark of OpenCFD Limited, producer and distributor of the OpenFOAM software. The author would also like to thanks the anonymous reviewers for their valuable comments.

7. Appendix A – The Effect of the Liquid Bridge Volume Model on Capillary Forces

The liquid bridge volume is an input parameter in almost the totality of models for calculating the capillary and viscous force between two wet particles. Thus, different models for liquid bridge volume will lead to different characteristics of the resulting cohesive force. Therefore, in this appendix, we attempt to quantify this difference by using our newly developed model. Specifically, we compute and compare the capillary force by using three different liquid bridge models: (1) the constant bridge model of Shi and McCarthy [42]; (2) the early bridge volume model presented in this paper; (3) and the bridge volume from our dynamic filling model considering the limit of infinitely long times.

In order to make a comparison, we pick the parameters of the particle system as follows:

- Initial film heights of $h_0^+ = 0.01$ (i.e., a thin film), and $h_0^+ = 0.1$ (i.e., thick film) are considered
- Particle ratio of $R_r = 0.5$
- Surface tension equal to 0.07 $N \cdot m^{-1}$

The constant liquid bridge volume is provided by the model of Shi and McCarthy [42]

$$V_b = \frac{L_{p1}}{2}\left(1-\sqrt{1-\frac{R_2^2}{\left(R_1+R_2\right)^2}}\right)+\frac{L_{p2}}{2}\left(1-\sqrt{1-\frac{R_1^2}{\left(R_1+R_2\right)^2}}\right) \qquad (A.1)$$

Where L_{p1} and L_{p2} are the initial liquid contents on particle 1 and particle 2, respectively. The total liquid bridge is composed of liquid from both contacting particles.

The early stage of liquid bridge is modelled by equation (12). To make the comparison easier, we use a case of zero separation to compute the initial bridge volume. We then simply calculate the initial bridge to be:

$$V_{b,0}^+ = 50.8 R_r^{-1.25}\left(h_0^+\right)^{2.15}. \qquad (A.2)$$

The maximum liquid bridge volume can be obtained by setting the filling time to $t^+ = \infty$, consequently the expressions of liquid bridge model in the Appendix A of our previous work [28] can be rewritten as:

$$V_b^+ = V_{b,0}^+ - C_1 \frac{\frac{2r_1}{a_i} + 2\phi_{m1}}{r_1} - C_2 \frac{\frac{2r_2}{a_i} + 2\phi_{m1}}{r_2} \tag{A.3}$$

$$r_1 = \frac{-a_i\left(\phi_{m1} + \phi_{m2} + 1 + \sqrt{\left(\phi_{m1} - \phi_{m2}\right)^2 + 1}\right)}{2} \tag{A.4}$$

$$r_2 = \frac{-a_i\left(\phi_{m1} + \phi_{m2} + 1 - \sqrt{\left(\phi_{m1} - \phi_{m2}\right)^2 + 1}\right)}{2} \tag{A.5}$$

$$\begin{aligned} C_1 = {} & \frac{-a_i^2\phi_{m2}L_{p2,0}^+ - \left(2a_i r_2\phi_{m1} + 2a_i^2\phi_{m1}^2 + a^2\phi_{m1}\right)L_{p1,0}^+}{2\left(r_2 - r_1\right)} \\ & + \frac{\left(a_i^2\phi_{m1} + a_i^2 + a_i r_2\right)V_{b,0}^+}{2\left(r_2 - r_1\right)} \end{aligned} \tag{A.6}$$

$$C_2 = \frac{a_i^2\phi_{m2}L_{p2,0}^+ + \left(2a_i r_1\phi_{m1} + a_i^2\phi_{m1} + 2a_i^2\phi_{m1}^2\right)L_{p1,0}^+ - \left(a_i r + a_i^2\phi_{m1} + a_i^2\right)V_{b,0}^+}{2\left(r_2 - r_1\right)} \tag{A.7}$$

Where $V_{b,0}^+$ is the initial bridge volume, $L_{p1,0}^+$ and $L_{p2,0}^+$ is the initial liquid content on the particle surfaces, and ϕ_{m1} and ϕ_{m2} can be calculated by using equations (20) and (23).

We employ the force model provided by Mikami et at. [20] to calculate the capillary force due to liquid bridge.

$$\begin{aligned} & F_{cap} = \pi R_2\sigma\left(e^{AS^+ + B} + C\right) \\ & A = -1.1\left(V_b^+\right)^{-0.53} \\ & B = \left(-0.34\ln\left(V_b^+\right) - 0.96\right)\theta^2 - 0.019\left(V_b^+\right) + 0.48 \\ & C = 0.0042\ln\left(V_b^+\right) + 0.078 \end{aligned} \tag{A.8}$$

Here S^+ is the surface to surface distance normalized by R_2 (R_2 is the size of the bigger particle, and θ is the contact angle which is assumed to be zero for our fully wet particle system). When a liquid bridge between particles reached a critical distance, the bridge

ruptures and liquid is redistributed. This rupture distance is given by Lian et al. [22], and reads:

$$h_{rup} = \left(1 + 0.5\theta\right)\left(V_b^+\right)^{1/3} \qquad (A.9)$$

The liquid bridge force is present as long as the bridge exists, and it vanishes when the liquid bridge ruptures at the critical rupture distance. The bridge forces are normalized by the capillary force scale $2\pi\sigma R_2$, and the rupture distance is scaled by R_2. The resulting capillary bridge force plots are shown in Figure A1.

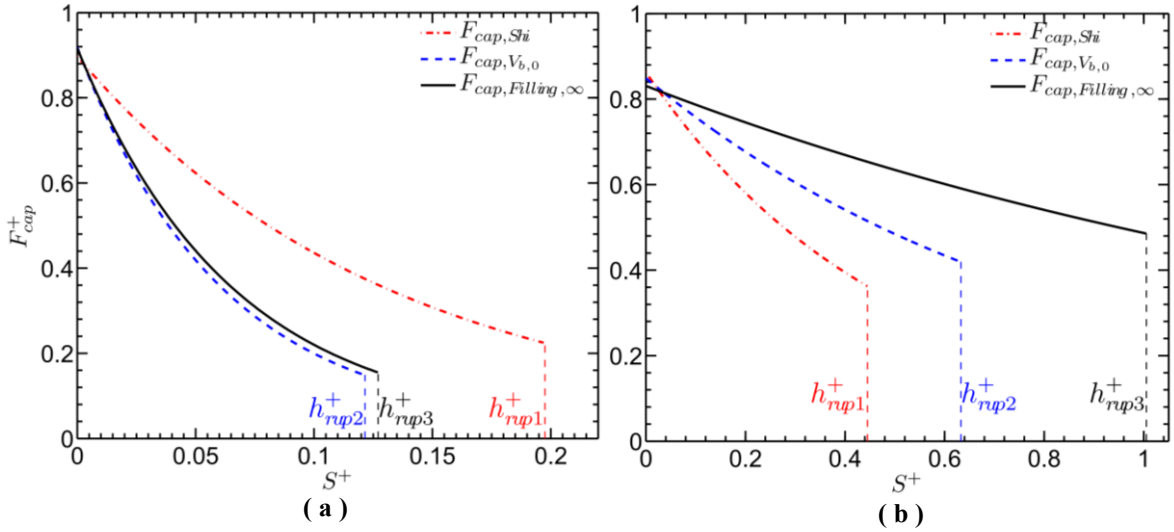

Figure A 1. The capillary bridge force versus the separation distance and critical rupture distance h_{rup}. h_{rup1} is the rupture distance based on the constant bridge model of Shi and McCarthy, h_{rup2} is the rupture distance based on our early stage bridge model, and h_{rup3} is the rupture distance based on the dynamic bridge model when the filing time t^+ is infinitely large . Panel (a) shows data with an initial film height of $h_0^+ = 0.01$; for panel (b) $h_0^+ = 0.1$

Figure A1 shows that the bridge forces are indeed affected by the liquid bridge volume model. Panel (a) indicates that there is not much difference between the bridge forces of our early stage bridge model and the dynamic filing model when particles are initialized with very small film heights. However, the model of Shi and McCarthy overpredicts the capillary bridge force when compared to our models. Panel (b) shows that the filling of the liquid bridge volume indeed affects the bridge force. The rupture distance in case the particles are initialized with a larger film height (i.e., $h_0^+ = 0.1$) differs for the different liquid bridge volume models: the dynamic bridge model predicts the biggest bridge force, as well as larger rupture distance.

Nomenclature

Latin Symbols

a_i .....Dimensionless filling rate parameter [-]

d_p .....Particle diameter of the larger particle [m]

g .....Gravity [m/s^2]

h_0 .....Average initial film height of the particle pair [m]

h_i .....Initial film height of particle i [m]

$L_{p,0}$ .....Reference volume of liquid on the particle [m³]

$L_{p,i}$ .....Volume of liquid present on the particle i [m³]

m .....Mass of the particle [kg]

$\mathbf{n}_{ij}$ .....Unit normal vector [-]

Oh .....Ohnesorge number [-]

p .....Pressure [Pa]

p_{ref} .....Reference pressure [Pa]

p_s .....Pressure at the particle surfaces [Pa]

p_{V_b} .....Pressure at the liquid bridge [Pa]

R_1 .....Particle radius of the smaller particle (particle 1)[m]

R_2 .....Particle radius of the larger particle (particle 2)[m]

R_{cyl} .....Radius of the initial cylinder region [m]

R_{curve} .....Radius of curvature of the liquid bridge surface [m]

Re .....Reynolds number [-]

S .....Half separation distance between particles [m]

t .....Time [s]

t_{acc} .....Acceleration time scale [s]

t_{cross} .....Film crossing time scale [s]

t_{relax} .....Particle relation time [s]

t_{ref} .....Reference time scale [s]

u_{ref} .....Reference fluid velocity [m·s]

u_{rel} .....Relative particle-particle velocity [m/s]

U .....Fluid velocity [m/s]

V_b .....Liquid bridge volume [m^3]

$V_{b,0}$ .....Initial bridge volume [m^3]

$V_{b,g}$ .....Geometrical bridge volume [m^3]

DIM.....Direct integration method

DNS .....Direct Numerical Simulation

DEM .....Discrete element method

YLE.....Young-Laplace equation

Greek Symbols

α .....Phase fraction indicator [-]

$\beta_{\mathrm{cyl,i}}$ .....Initial filling angle on particle *i* that cause by geometry bride [rad]

Δt .....Time step [s]

Δx .....Grid spacing [m]

Δh .....Dimensionless grid spacing by initial film height [-]

ϕ_p .....Particle volume fraction [-]

ϕ_{mi} .....Fraction of liquid on particle *i* that is mobile to flow into the bridge [-]

μ_l .....Dynamic viscosity of liquid [$kg \cdot m^{-1} \cdot s^{-1}$]

μ_g .....Dynamic viscosity of ambient gas [$kg \cdot m^{-1} \cdot s^{-1}$]

ρ_l .....Density of the liquid [$kg \cdot m^{-3}$]

ρ_g .....Density of the ambient gas [kg · m^{-3}]

ρ_p .....Density of the particles [kg · m^{-3}]

σ .....Surface tension [kg · s^{-2}]

Superscripts

+ .....Dimensionless quantity

i .....Particle index

norm .....Normal direction

tang .....Tangential direction

t .....Terminal

w .....Water

gly .....Glycerine

p .....Particle

ref .....Reference quantity

8. References

[1] C.K. Gupta, D. Sathiyamoorthy, Fluid Bed Technology in Materials Processing, CRC Press, 1998.

[2] D. Kunii, O. Levenspiel, Fluidization Engineering, Butterworth-Heinemann, 1991.

[3] H. Xu, W. Zhong, A. Yu, Z. Yuan, Spouting Characteristics of Wet Particles in a Conical-Cylindrical Spouted Bed, Ind. Eng. Chem. Res. 54 (2015) 9894–9902. doi:10.1021/acs.iecr.5b02742.

[4] M.G. Rasul, V. Rudolph, M. Carsky, Segregation potential in binary gas fluidized beds, Powder Technol. 103 (1999) 175–181. doi:10.1016/S0032-5910(98)00230-7.

[5] M. Wormsbecker, A. Adams, T. Pugsley, C. Winters, Segregation by size difference in a conical fluidized bed of pharmaceutical granulate, Powder Technol. 153 (2005) 72–80. doi:10.1016/j.powtec.2005.02.006.

[6] R. Fan, R.O. Fox, Segregation in polydisperse fluidized beds: Validation of a multi-fluid model, Chem. Eng. Sci. 63 (2008) 272–285. doi:10.1016/j.ces.2007.09.038.

[7] S.Y. Wu, J. Baeyens, Segregation by size difference in gas fluidized beds, Powder Technol. 98 (1998) 139–150. doi:10.1016/S0032-5910(98)00026-6.

[8] G. Sun, J.R. Grace, The effect of particle size distribution on the performance of a catalytic fluidized bed reactor, Chem. Eng. Sci. 45 (1990) 2187–2194. doi:10.1016/0009-2509(90)80094-U.

[9] H. Hatzantonis, C. Kiparissides, The effect of the mean particle size on the dynamic behaviour of catalyzed olefin polymerization fluidized bed reactors, Comput. Chem. Eng. 22 (1998) S127–S134. doi:10.1016/S0098-1354(98)00046-5.

[10] V. Wilk, H. Hofbauer, Influence of fuel particle size on gasification in a dual fluidized bed steam gasifier, Fuel Process. Technol. 115 (2013) 139–151. doi:10.1016/j.fuproc.2013.04.013.

[11] J. Werther, Scale-up modeling for fluidized bed reactors, Chem. Eng. Sci. 47 (1992) 2457–2462. doi:10.1016/0009-2509(92)87076-3.

[12] C.M. Donahue, C.M. Hrenya, R.H. Davis, Stokes's cradle: Newton's cradle with liquid coating, Phys. Rev. Lett. 105 (2010) 34501. doi:10.1103/PhysRevLett.105.034501.

[13] S. Herminghaus, Dynamics of wet granular matter, Adv. Phys. 54 (2005) 221–261. doi:10.1080/00018730500167855.

[14] C. Voivret, F. Radjaï, J.Y. Delenne, M.S. El Youssoufi, Multiscale force networks in highly polydisperse granular media, Phys. Rev. Lett. 102 (2009). doi:10.1103/PhysRevLett.102.178001.

[15] J.K. Mitchell, K. Soga, Soil Composition and Engineering Properties, in: Fundam. Soil Behav., 2005: pp. 83–108.

[16] F. Radjai, V. Richefeu, Bond anisotropy and cohesion of wet granular materials., Philos. Trans. A. Math. Phys. Eng. Sci. 367 (2009) 5123–5138. doi:10.1098/rsta.2009.0185.

[17] G. Toschkoff, J.G. Khinast, Mathematical modeling of the coating process., Int. J. Pharm. 457 (2013) 407–22. doi:10.1016/j.ijpharm.2013.08.022.

[18] K. Hotta, K. Iinoya, The capillary binding force of a liquid bridge, Powder Technol. 12

(1975) 195. doi:10.1016/0032-5910(75)80014-3.

[19] H. Xu, W. Zhong, Z. Yuan, A. Yu, CFD-DEM study on cohesive particles in a spouted bed, Powder Technol. (2016). doi:10.1016/j.powtec.2016.09.006.

[20] T. Mikami, H. Kamiya, M. Horio, Numerical simulation of cohesive powder behavior in a fluidized bed, Chem. Eng. Sci. 53 (1998) 1927–1940. doi:10.1016/S0009-2509(97)00325-4.

[21] P. Pierrat, H.S. Caram, Tensile strength of wet granular materials, Powder Technol. 91 (1997) 83–93. doi:10.1016/S0032-5910(96)03179-8.

[22] G. Lian, C. Thornton, M.J. Adams, A Theoretical Study of the Liquid Bridge Forces between Two Rigid Spherical Bodies, J. Colloid Interface Sci. 161 (1993) 138–147. doi:http://dx.doi.org/10.1006/jcis.1993.1452.

[23] M. Urso, C. Lawrence, M. Adams, Pendular, Funicular, and Capillary Bridges: Results for Two Dimensions., J. Colloid Interface Sci. 220 (1999) 42–56. doi:10.1006/jcis.1999.6512.

[24] C.D. Willett, M.J. Adams, S.A. Johnson, J.P.K. Seville, Capillary bridges between two spherical bodies, Langmuir. 16 (2000) 9396–9405. doi:10.1021/la000657y.

[25] M.A. Erle, D.C. Dyson, N.R. Morrow, Liquid bridges between cylinders, in a torus, and between spheres, AIChE J. 17 (1971) 115–121. doi:10.1002/aic.690170125.

[26] Y.I. Rabinovich, M.S. Esayanur, B.M. Moudgil, Capillary forces between two spheres with a fixed volume liquid bridge: Theory and experiment, Langmuir. 21 (2005) 10992–10997. doi:10.1021/la0517639.

[27] J. Sprakel, N.A.M. Besseling, M.A. Cohen Stuart, F.A.M. Leermakers, Capillary adhesion in the limit of saturation: Thermodynamics, self-consistent field modeling and experiment, Langmuir. 24 (2008) 1308–1317. doi:10.1021/la702222f.

[28] M. Wu, S. Radl, J.G. Khinast, A model to predict liquid bridge formation between wet particles based on direct numerical simulations, AIChE J. 62 (2016) 1877–1897. doi:10.1002/aic.15184.

[29] F.M. Orr, L.E. Scriven, A.P. Rivas, Pendular rings between solids: meniscus properties and capillary force, J. Fluid Mech. 67 (1975) 723. doi:10.1017/S0022112075000572.

[30] F. Soulié, F. Cherblanc, M.S. El Youssoufi, C. Saix, Influence of liquid bridges on the mechanical behaviour of polydisperse granular materials, Int. J. Numer. Anal. Methods Geomech. 30 (2006) 213–228. doi:10.1002/nag.476.

[31] V. Richefeu, M.S. El Youssoufi, R. Peyroux, F. Radjaï, A model of capillary cohesion for numerical simulations of 3D polydisperse granular media, Int. J. Numer. Anal. Methods Geomech. 32 (2008) 1365–1383. doi:10.1002/nag.674.

[32] Y. Chen, Y. Zhao, H. Gao, J. Zheng, Liquid bridge force between two unequal-sized spheres or a sphere and a plane, Particuology. 9 (2011) 374–380. doi:10.1016/j.partic.2010.11.006.

[33] O. Harireche, A. Faramarzi, A.M. Alani, A toroidal approximation of capillary forces in polydisperse granular assemblies, Granul. Matter. 15 (2013) 573–581. doi:10.1007/s10035-013-0425-9.

[34] V.P. Mehrotra, K.V.S. Sastry, Pendular Bond Strength Between Unequal-Sized Spherical Particles, Powder Technol. 25 (1980) 203–214.

[35] S.J.R. Simons, J.P.K. Seville, M.J. Adams, An analysis of the rupture energy of pendular liquid bridges, Chem. Eng. Sci. 49 (1994) 2331–2339. doi:10.1016/0009-

2509(94)E0050-Z.

[36] L.A. Easo, R. Kumar, R. Ren, R. Carl, Numerical Study of the Formation of a Liquid Bridge Between Two Spheres with Uniform Film Thickness, in: 2014 AICHE Annu. Meet. Novemb. 18, Atlanta, 2014.

[37] Wu, M and Khinast, J G and S, Radl, Towards A Refined Model for Liquid Bridge Volume Between Wet Particles, in: 11th. World Congr. Comput. Mech. (WCCM XI), Barcelona, Spain, 2014.

[38] S.S. Deshpande, L. Anumolu, M.F. Trujillo, Evaluating the performance of the two-phase flow solver interFoam, Comput. Sci. Discov. 5 (2012) 14016. doi:10.1088/1749-4699/5/1/014016.

[39] a. Eddi, K.G. Winkels, J.H. Snoeijer, Short time dynamics of viscous drop spreading, Phys. Fluids. 25 (2013) 13102. doi:10.1063/1.4788693.

[40] S. Radl, S. Sundaresan, A drag model for filtered Euler-Lagrange simulations of clustered gas-particle suspensions, Chem. Eng. Sci. 117 (2014) 416–425. doi:10.1016/j.ces.2014.07.011.

[41] C. Kloss, C. Goniva, A. Hager, S. Amberger, S. Pirker, Models , algorithms and validation for opensource DEM and CFD-DEM, Prog. Comput. Fluid Dyn. 12 (2012) 140–152. doi:10.1504/PCFD.2012.047457.

[42] D. Shi, J.J. McCarthy, Numerical simulation of liquid transfer between particles, Powder Technol. 184 (2008) 64–75. doi:10.1016/j.powtec.2007.08.011.

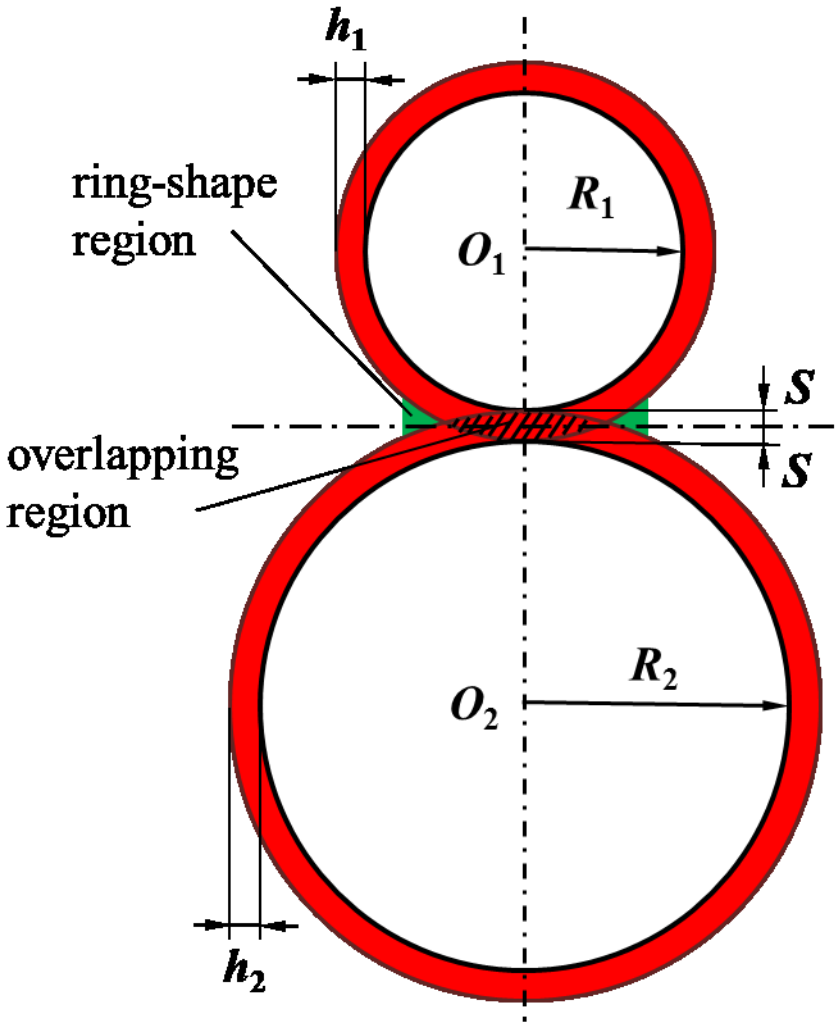

Figure 1: Particle configuration, and illustration of the calculation of the initial bridge shape.

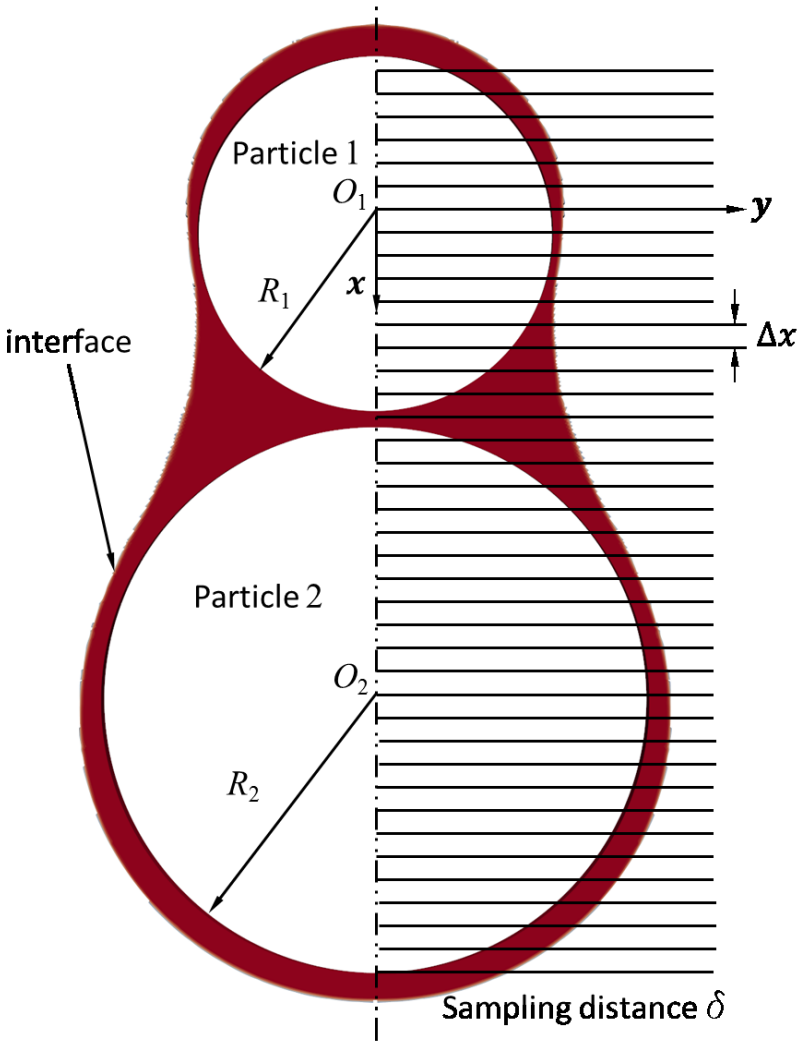

Figure 2: Sketch of the sampling approach used to detected neck positions on the large and small particle.

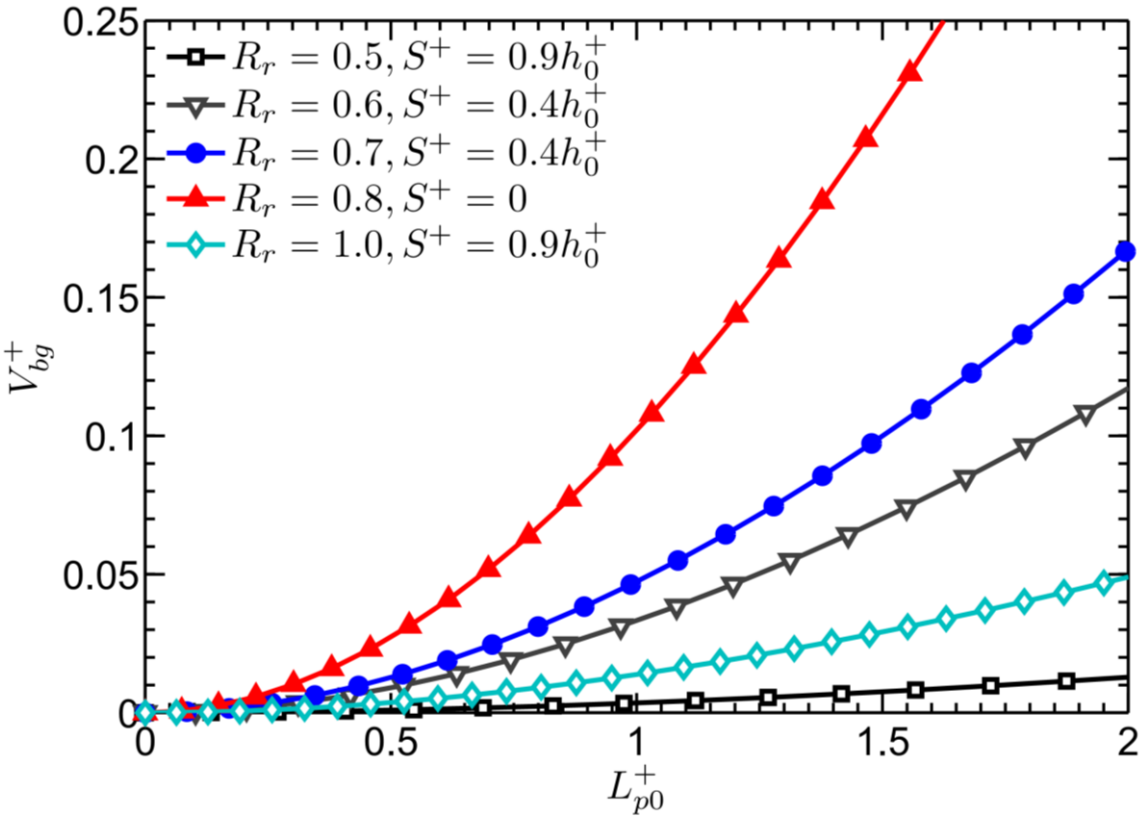

Figure 3: Effects of the separation distance and particle size on the bridge volume as function of initial liquid content, L_{p0}^{+} is the average initial liquid content on particles, V_{bg}^{+} is the total geometrical bridge volume.

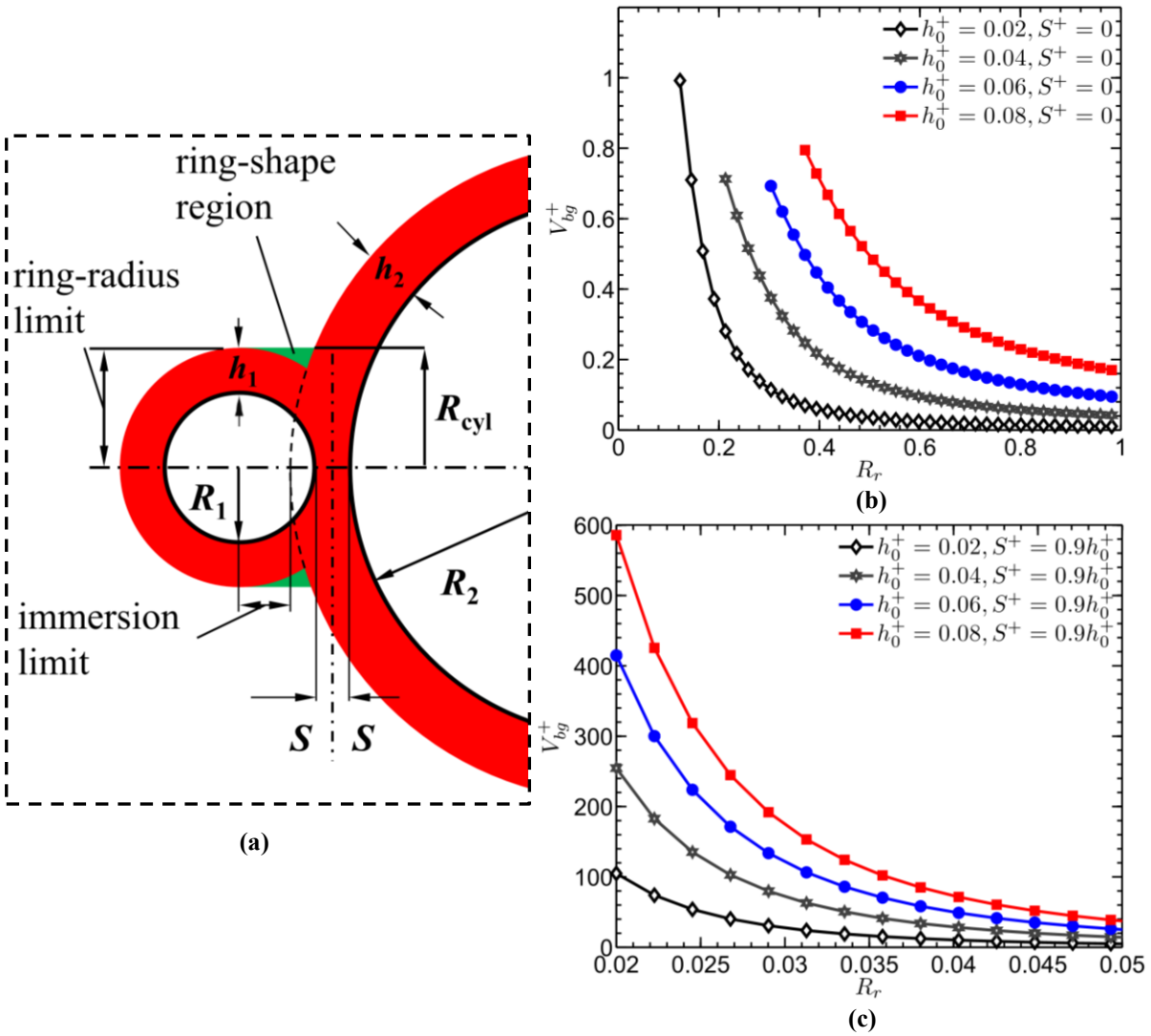

Figure 4: Geometrical bridge volume versus particle size ratio R_r. Panel (a) illustrates the limiting case when a small particle becomes immersed in the liquid layer of the larger particle. Panel (b): geometrical bridge volume versus particle size ratio R_r with different initial film heights and zero separations. Panel (c): geometrical bridge volume versus particle size ratio R_r with different initial film heights and larger separations. h_0 is the average initial film height, and we have chosen $h_0 = h_1 = h_2$.

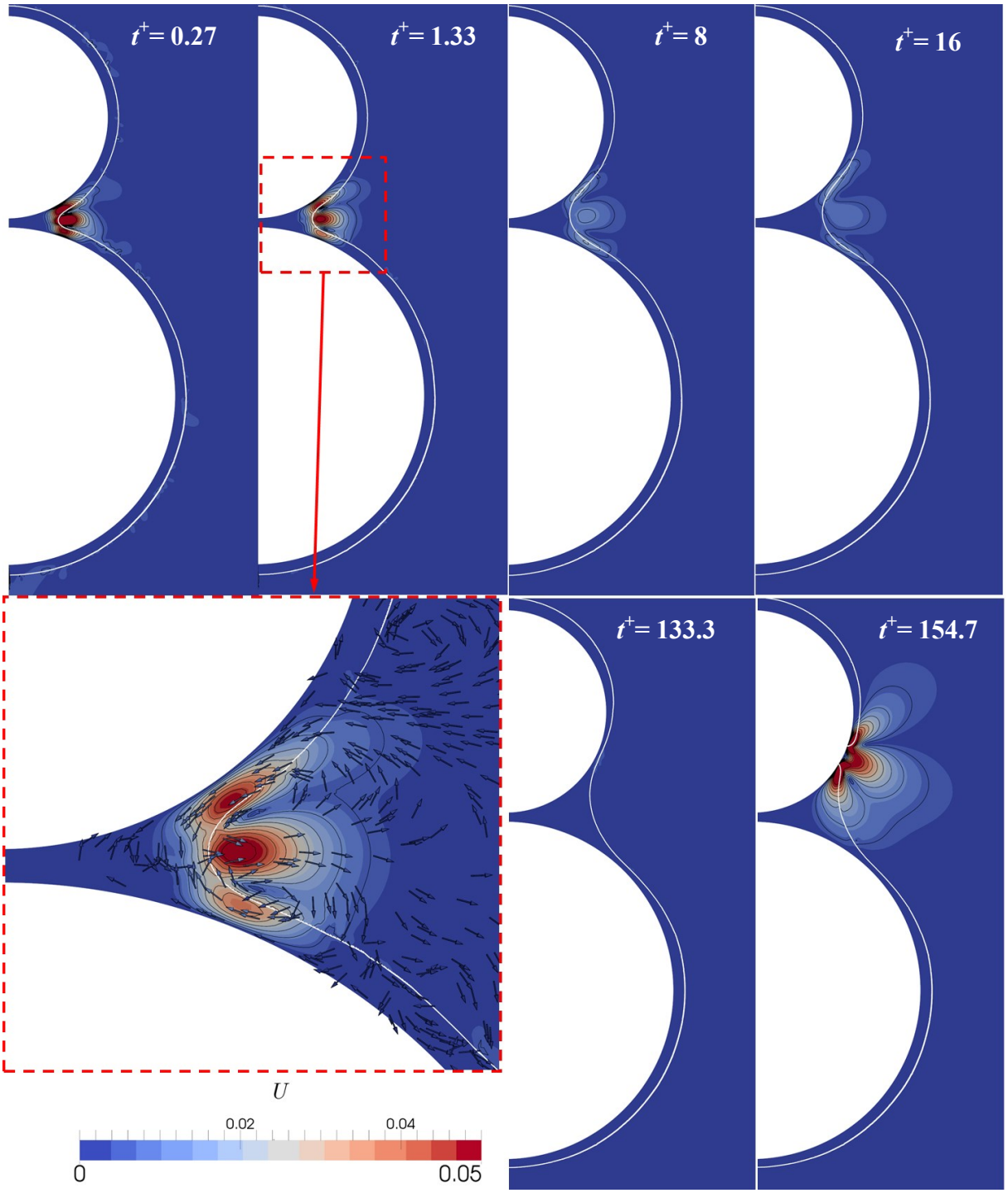

Figure 5: Typical velocity field for liquid transport from the particles' surface to the bridge region between two unequally-sized particles ($R_1 = 0.6$, $R_2 = 1$, $S^+ = 0.027$, $h_0 = h_1 = h_2 = 0.06\ R_2$).

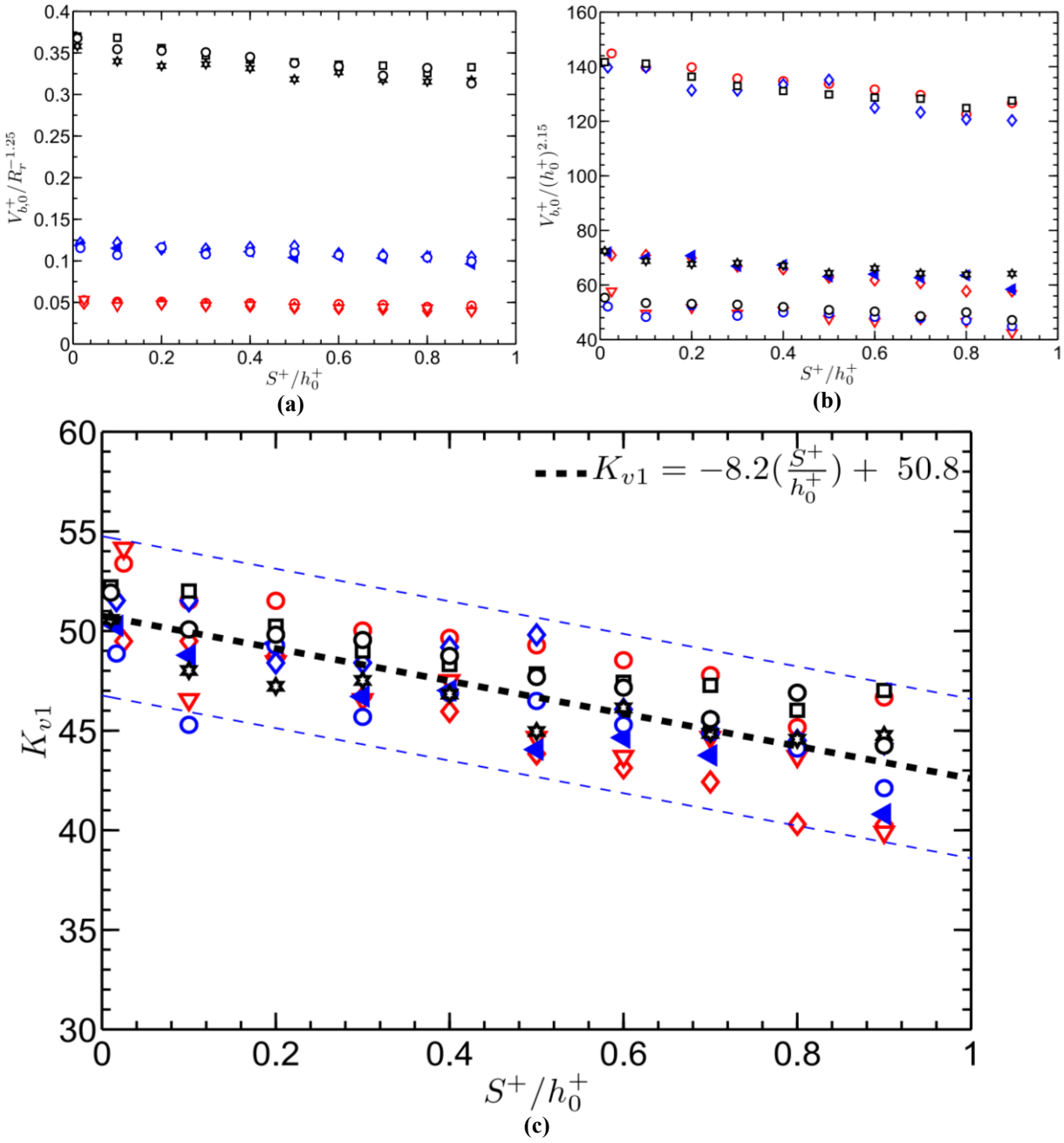

Figure 6: Initial bridge model (K_{v1}) coefficient based on different particle radius ratio (R_r) and initial film height (h_0) vs. normalized separation distance. Panel (a): initial bridge volume normalized with $R_r^{-1.25}$ for different initial film highs, red markers: initial film high h_0 = 0.04 R_2, blue markers: h_0 = 0.06 R_2, black markers: h_0 = 0.1 R_2. Panel (b): initial bridge volume normalized to $h_0^{2.15}$ for different particle-radius ratios, from top to bottom, R_r = 0.45, R_r = 0.75 and R_r = 0.95. Panel (c) initial bridge volume normalized with both $R_r^{-1.25}$ and $h_0^{2.15}$. The thin dashed lines indicate an error of +/- 8%. Red circles: R_r = 0.45 and h_0^+ = 0.04; Red diamonds: R_r = 0.75 and h_0^+ = 0.04; Red triangles: R_r = 0.95 and h_0^+=0.04. Blue diamonds: R_r = 0.45 and h_0^+ = 0.06; Blue left triangles: R_r = 0.75 and h_0^+ = 0.06; Blue circles: R_r = 0.95 and h_0^+ = 0.06. Black squares: R_r = 0.45 and h_0^+ = 0.1; Black hexagrams: R_r = 0.75 and h_0^+ = 0.1; Black circles: R_r = 0.95 and h_0^+ = 0.1.

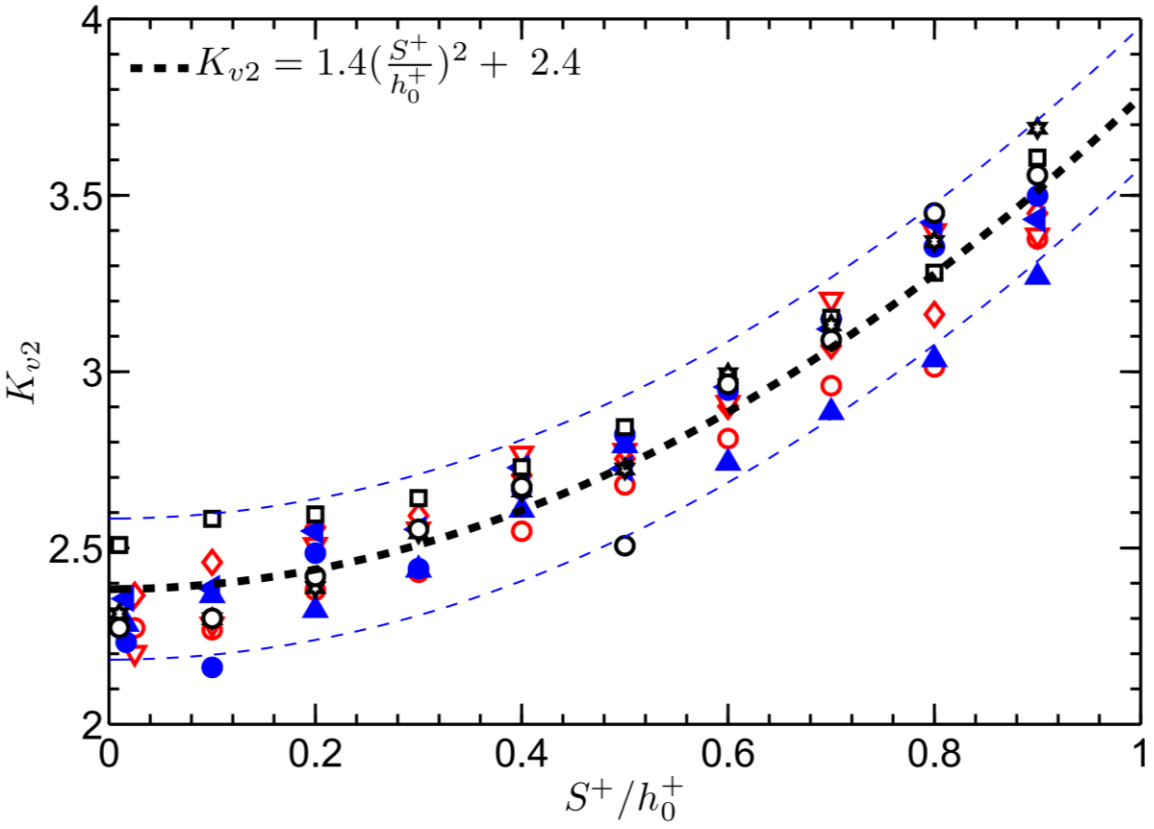

Figure 7: Initial bridge model (K_{v2}) coefficient based on different radius ratio (R_r) and initial film high (h_0) vs. normalized separation distance. The thin dashed lines indicate an error of +/- 8%. (Red circles: R_r = 0.45 and h_0^+ = 0.04; Red diamonds: R_r = 0.75 and h_0^+ = 0.04; Red triangles: R_r = 0.95 and h_0^+=0.04. Blue up triangles: R_r = 0.45 and h_0^+ = 0.06; Blue left triangles: R_r = 0.75 and h_0^+ = 0.06; Blue circles: R_r = 0.95 and h_0^+ = 0.06. Black squares: R_r = 0.45 and h_0^+ = 0.1; Black hexagrams: R_r = 0.75 and h_0^+ = 0.1; Black circles: R_r = 0.95 and h_0^+ = 0.1)

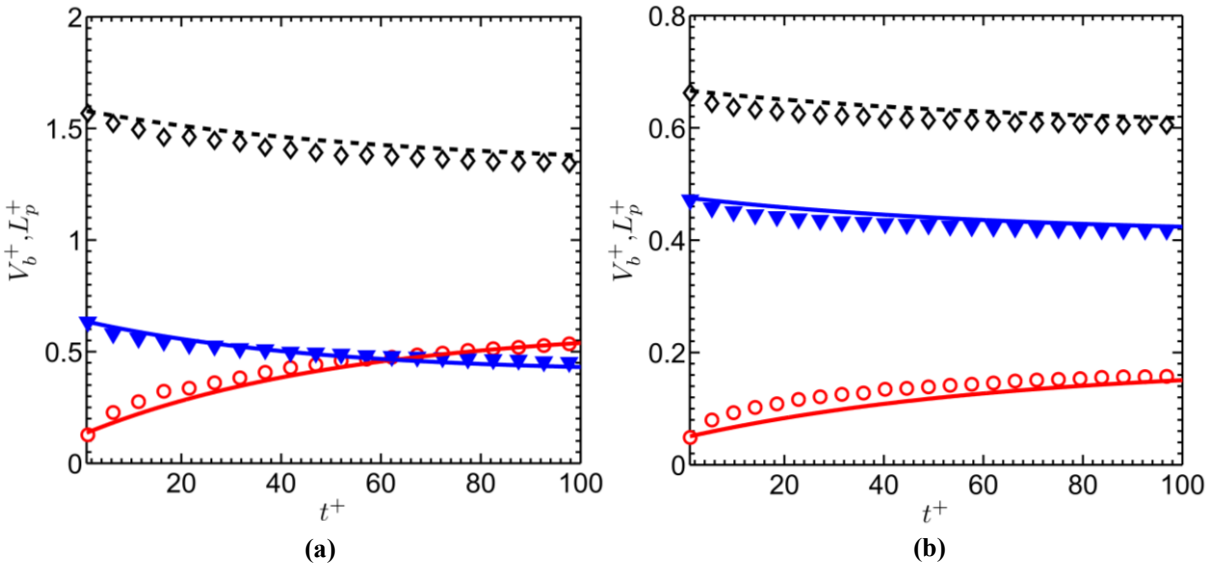

Figure 8: Fitted model (lines) vs. DNS data (symbols) over time; Red circles: liquid bridge volume (V_b^+); Blue triangles: liquid content on particle 1 (L_{p1}^+); Black diamonds: liquid content on particle 2 (L_{p2}^+); panel (a): R_r = 0.65, S^* = 0.018, and h_0 = 0.06 R_2 ; panel (b): R_r = 0.85, S^* = 0.012, and h_0 = 0.04 R_2

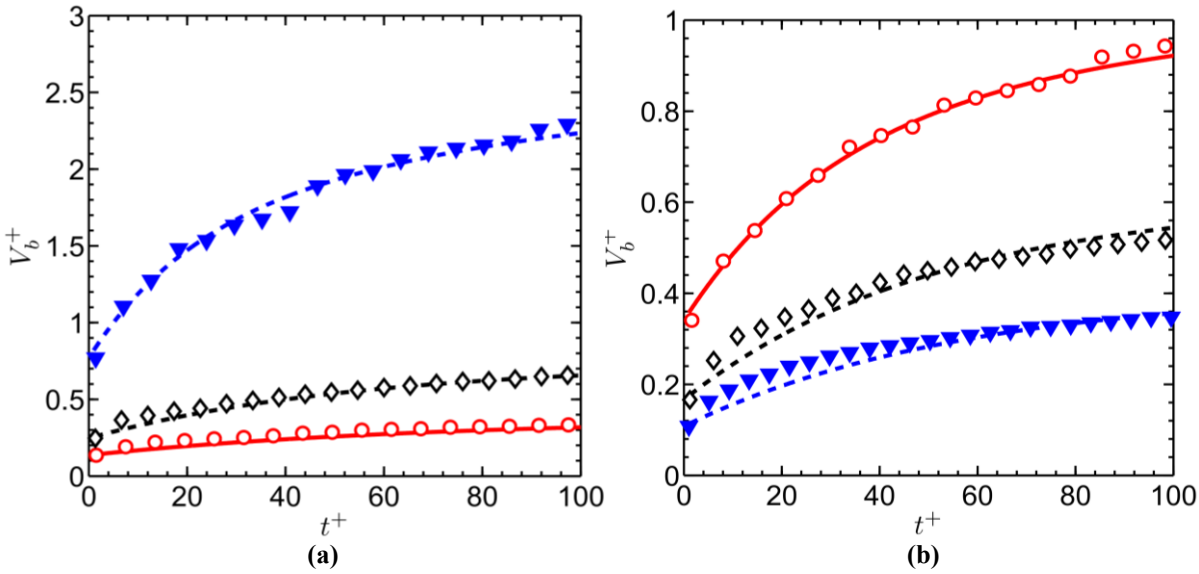

Figure 9: Liquid bridge volume over time: fitted model (lines) vs. DNS data (symbols). Panel (a): Red circles: R_r = 0.5, S^+ = 0, h_0^+ = 0.04; Black diamonds: R_r = 0.6, S^+ = 0, h_0^+ = 0.06; Blue triangles: R_r = 0.55, S^+ = 0.005, h_0^+ = 0.1. Panel (b): Red circles: R_r = 0.45, S^+ = 0.018, h_0^+ = 0.06; Black diamonds: R_r = 0.7, S^+ = 0.018, h_0^+ = 0.06; Blue triangles: R_r = 0.95, S^+ = 0.018, h_0^+ = 0.06

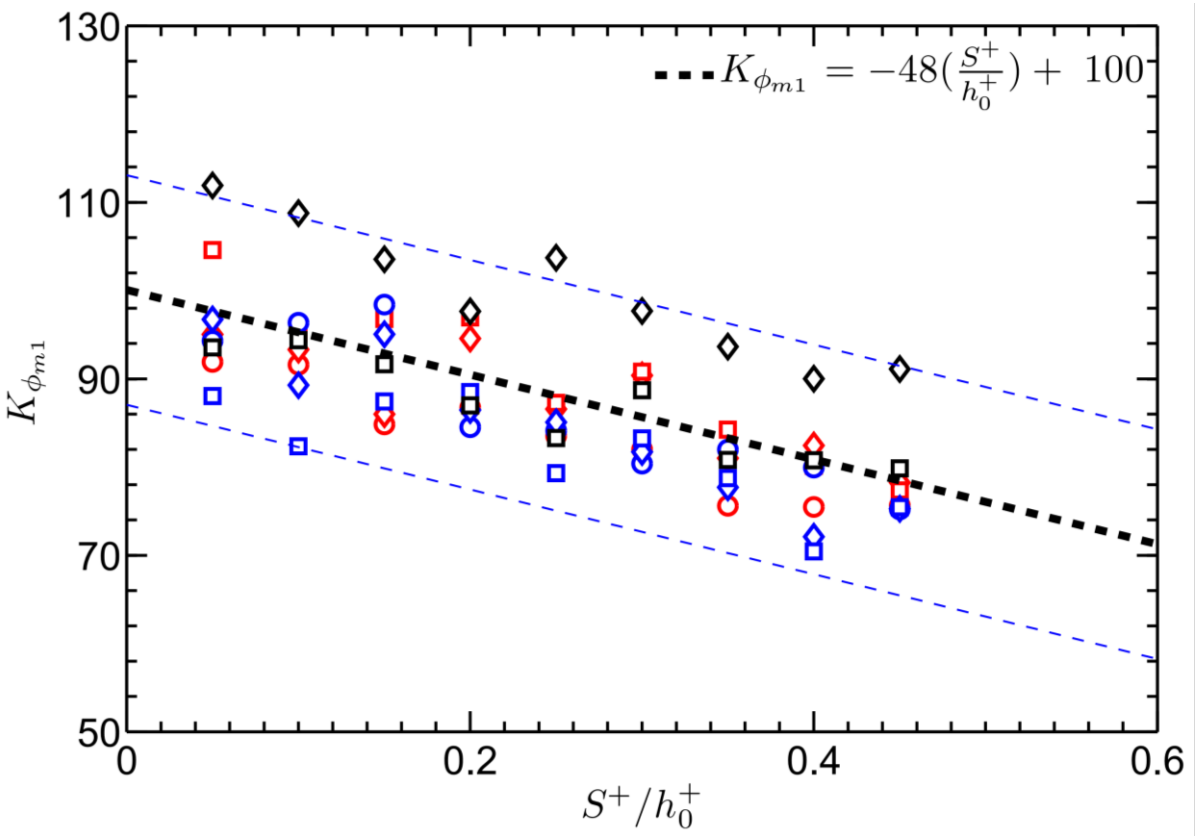

Figure 10: $K_{\phi_{m1}}$ **as function of separation *S* for different particle ratios. The thin dashed lines indicate an error of +/- 13%. (Red circles: R_r = 0.5 and h_0^+ = 0.04; Red diamonds: R_r = 0.7 and h_0^+ = 0.04; Red squares: R_r = 0.9 and h_0^+=0.04. Blue circles: R_r = 0.5 and h_0^+ = 0.06; Blue diamonds: R_r = 0.7 and h_0^+ = 0.06; Blue squares: R_r = 0.9 and h_0^+ = 0.06. Black circles: R_r = 0.5 and h_0^+ = 0.1; Black diamonds: R_r = 0.7 and h_0^+ = 0.1; Black squares: R_r = 0.9 and h_0^+ = 0.1)**

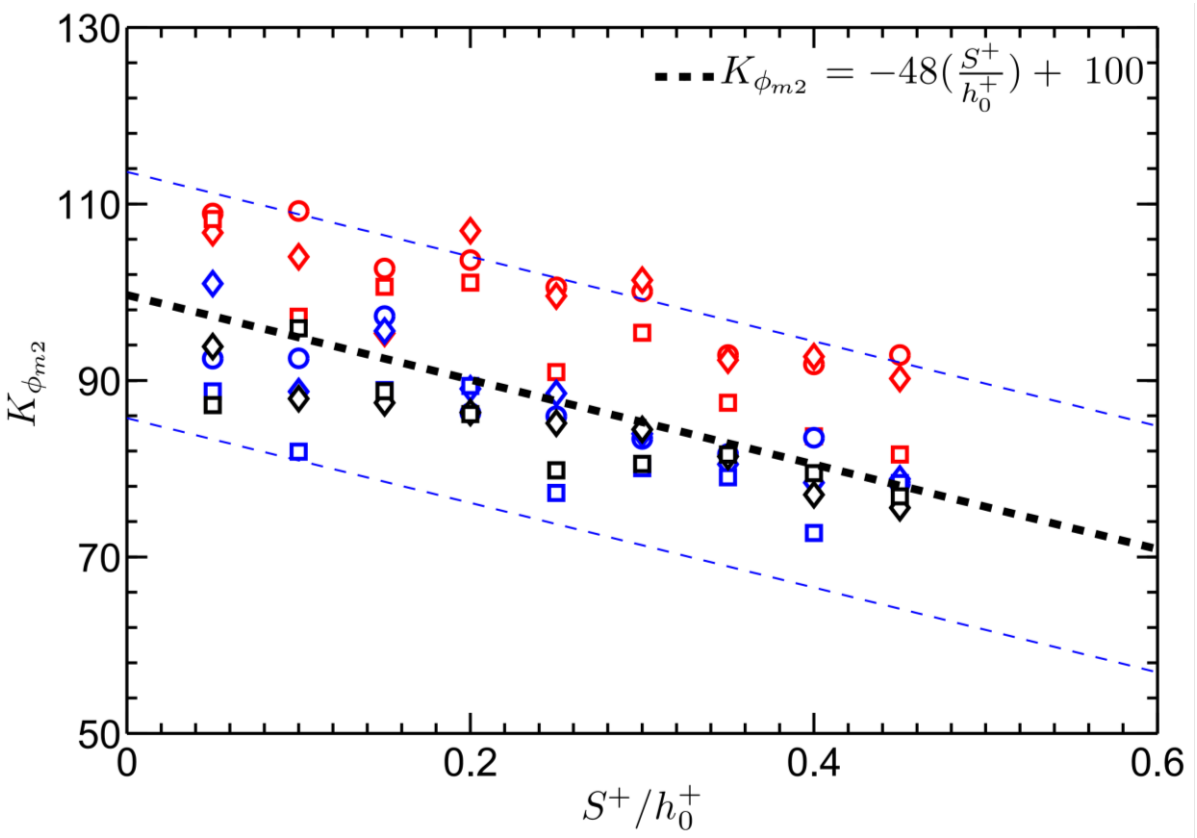

Figure 11: $K_{\phi_{m2}}$ **as function of separation *S* for different particle ratios. The thin dashed lines indicate an error of +/- 13%. (Red circles: R_r = 0.5 and h_0^+ = 0.04; Red diamonds: R_r = 0.7 and h_0^+ = 0.04; Red squares: R_r = 0.9 and h_0^+=0.04. Blue circles: R_r = 0.5 and h_0^+ = 0.06; Blue diamonds: R_r = 0.7 and h_0^+ = 0.06; Blue squares: R_r = 0.9 and h_0^+ = 0.06. Black circles: R_r = 0.5 and h_0^+ = 0.1; Black diamonds: R_r = 0.7 and h_0^+ = 0.1; Black squares: R_r = 0.9 and h_0^+ = 0.1)**

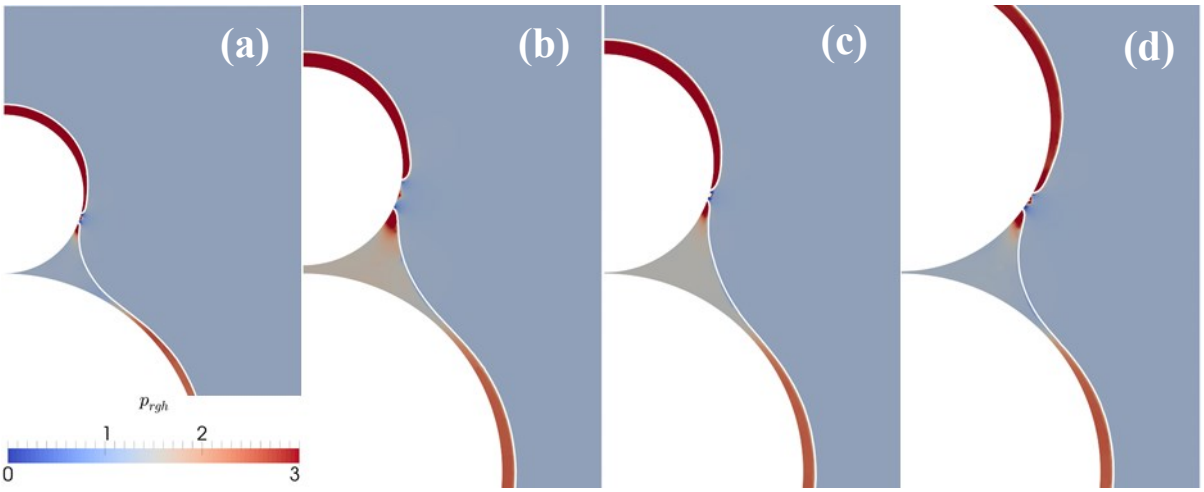

Figure 12: Pressure distribution of film rupture for different particle ratios, separation and film heights. Panel (a): R_r = 0.4, S^+ = 0, h_0^+ = 0.04; panel (b): R_r = 0.5, S^+ = 0.021, h_0^+ = 0.06; panel (c): R_r = 0.55, S^+= 0.003, h_0^+ = 0.06; panel (d): R_r = 0.75, S^+ = 0.006, h_0^+ = 0.06.

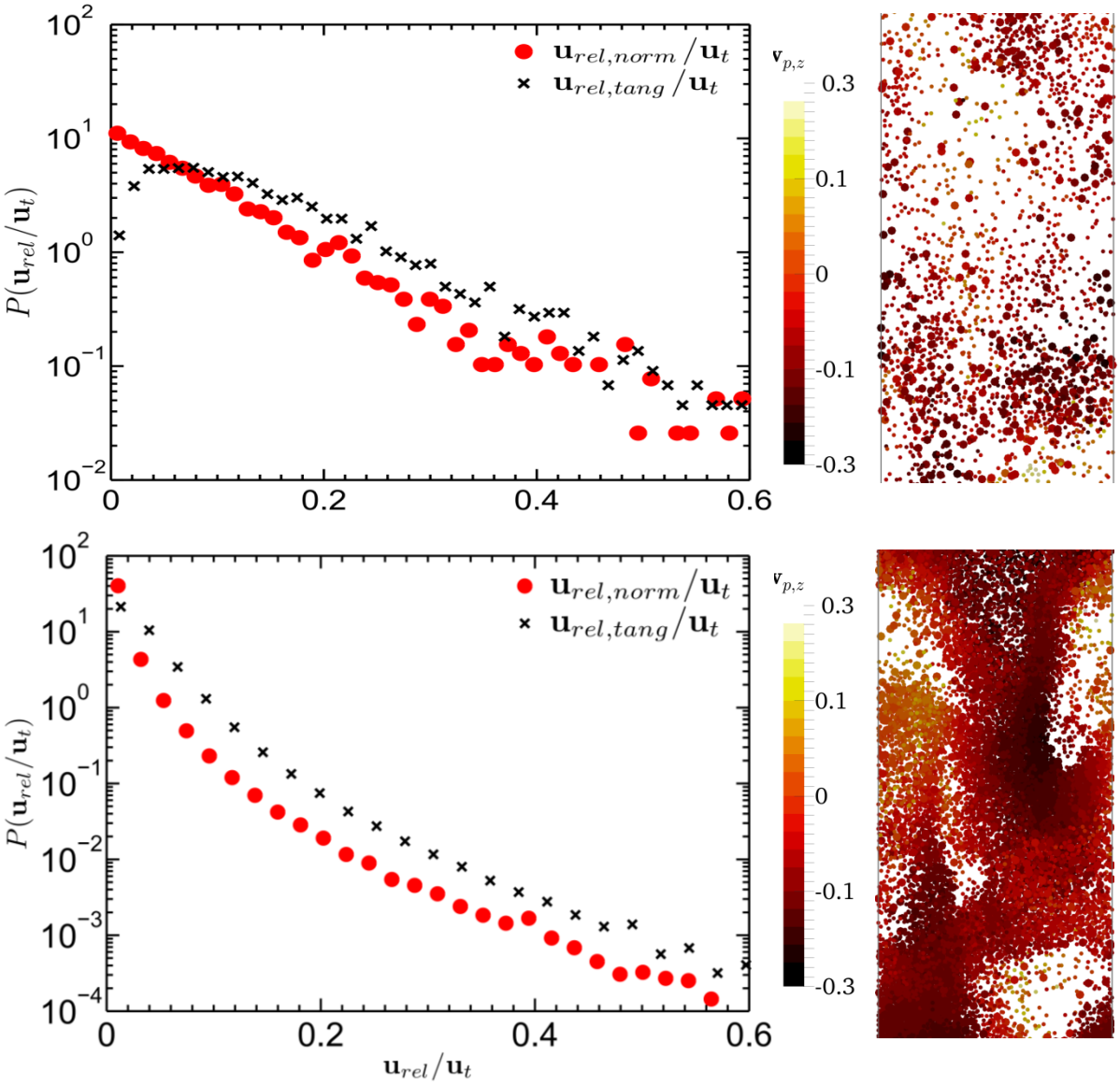

Figure 13: Distribution of polydisperse particle collision velocities in the normal and tangential direction, as well as illustration of the vertical velocity distribution (bottom panel: $R_r = 0.5$, $\phi_p = 0.3$) and dense (top panel; $R_r = 0.5$, $\phi_p = 0.05$) cloud of freely sedimenting particles (the inserts illustrate individual-particle velocities in the vertical direction).

Parameter	Value	Comment
Δt^+	$5 \cdot 10^{-3}$	Dimensionless time step
Δh	0.05 - 0.33	Dimensionless mesh resolution
Time derivative scheme	backward	Second order, implicit
Laplacian scheme	Gauss linear corrected	Unbounded, second order, conservative
Convection scheme (for U)	Gauss linear	Unbounded, second order
Convection scheme (for α)	Gauss vanLeer	van Leer limiter

Table 1: Simulation parameters and numerical schemes used in the VoF simulations.

Mixture	μ [Pa·s]	ρ [kg·m-3]	σ [N/m]
Water	1.10-3	1000	0.073
Glycerine/water-60/40%	0.0115	1153	0.0673
Glycerine/water-79/21%	0.05	1204	0.0647
Glycerine/water-90/10%	0.22	1238	0.0634
Pure glycerine	1.12	1262	0.0631

Table 2: Properties of different water-glycerine mixtures.

Glycerine/water	R_1 $[m]$	R_r	$\rho_p[kg \cdot m^{-3}]$	h_0^+	t_{ref} $[s]$	t_{acc}^+	t_{cross}^+	Oh
water	5e-6	0.5	1000	0.01	9.15e-8	273	363	0.045
Glycerine/water-60/40%	5e-6	0.5	1000	0.01	1.14e-6	1.91	29.2	0.51
Glycerine/water-79/21%	5e-6	0.5	1000	0.01	5.15e-6	0.097	6.45	2.38
Glycerine/water-90/10%	5e-6	0.5	1000	0.01	2.31e-5	4.91e-3	1.44	9.62
Pure glycerine	5e-6	0.5	1000	0.01	1.18e-5	1.89e-4	0.28	48.6
Water	1e-5	0.7	2000	0.04	1.61e-7	1240	147	0.034
Glycerine/water-60/40%	1e-5	0.7	2000	0.04	2.01e-6	8.65	11.8	0.38
Glycerine/water-79/21%	1e-5	0.7	2000	0.04	9.09e-6	0.44	2.61	1.79
Glycerine/water-90/10%	1e-5	0.7	2000	0.04	4.08e-5	0.022	0.58	7.24
Pure glycerine	1e-5	0.7	2000	0.04	2.09e-4	8.55e-4	0.11	36.7
Water	1e-5	0.9	5000	0.1	1.44e-7	3450	128	0.036
Glycerine/water-60/40%	1e-5	0.9	5000	0.1	1.80e-6	24.2	10.3	0.4
Glycerine/water-79/21%	1e-5	0.9	5000	0.1	8.13e-6	1.23	2.27	1.75
Glycerine/water-90/10%	1e-5	0.9	5000	0.1	3.65e-5	0.062	0.51	7.65
Pure glycerine	1e-5	0.9	5000	0.1	1.87e-4	2.39e-3	0.1	38.7

Table 3: Summary of parameters relevant for liquid transfer in typical polydisperse particle beds

Parameter	Value
Domain size – x (m)	$53 \cdot d_p$
Domain size – y (m)	$53 \cdot d_p$
Domain size – z (m)	$213 \cdot d_p$
Boundary conditions	Fully periodic
Gravitational acceleration: g (m/s^2)	9.81
The larger particle diameter of the system: d_p (m)	$1.50 \cdot 10^{-4}$
Particle density: ρ_p (kg/m^3)	1,500
Gas density: ρ_g (kg/m^3)	1.3
Gas viscosity: μ_g (Pa·s)	1.8×10^{-5}

Table 4: System parameters and boundary conditions used in the simulations of a freely sedimenting bi-disperse particle suspension.